Draft version February 19, 2024
Typeset using LaTeX default style in AASTeX62

Statistical Study of Gamma-Ray Bursts with a Plateau Phase in the X-ray Afterglow

Chen-Han Tang,[1] Yong-Feng Huang,[1,2] Jin-Jun Geng,[1] and Zhi-Bin Zhang[3]

[1] *School of Astronomy and Space Science, Nanjing University*
Nanjing 210023, P. R. China
[2] *Key Laboratory of Modern Astronomy and Astrophysics (Nanjing University)*
Ministry of Education, P. R. China
[3] *College of Physics and Engineering, Qufu Normal University*
Qufu 273165, P. R. China

(Received February 19, 2024; Revised February 19, 2024; Accepted February 19, 2024)

ABSTRACT

A plateau phase in the X-ray afterglow is observed in a significant fraction of gamma-ray bursts (GRBs). Previously, it has been found that there exists a correlation among three key parameters concerning the plateau phase, i.e., the end time of the plateau phase in the GRB rest frame (T_a), the corresponding X-ray luminosity at the end time (L_X) and the isotropic energy of the prompt GRB ($E_{\gamma,\rm iso}$). In this study, we systematically search through all the *Swift* GRBs with a plateau phase that occurred between 2005 May and 2018 August. We collect 174 GRBs, with redshifts available for all of them. For the whole sample, the correlation between L_X, T_a and $E_{\gamma,\rm iso}$ is confirmed, with the best fit relation being $L_X \propto T_a^{-1.01} E_{\gamma,\rm iso}^{0.84}$. Such an updated three-parameter correlation still supports that the central leftover after GRBs is probably a millisecond magnetar. It is interesting to note that short GRBs with duration less than 2 s in our sample also follow the same correlation, which hints that the merger production of two neutron stars could be a high mass magnetar, but not necessarily a black hole. Moreover, GRBs having an "internal" plateau (i.e., with a following decay index being generally smaller than -3) also obey this correlation. It further strengthens the idea that the internal plateau is due to the delayed collapse of a high mass neutron star into a black hole. The updated three-parameter correlation indicates that GRBs with a plateau phase may act as a standard candle for cosmology study.

Keywords: gamma-ray burst: general – methods: statistical

1. INTRODUCTION

Gamma-ray bursts (GRBs) are erratic γ-ray flashes in the universe, lasting from milliseconds to as long as thousands of seconds[1], usually with a non-thermal spectrum, isotropically distributed on the sky (Band et al. 1993; Kouveliotou et al. 1993; Meegan et al. 1992). The isotropic energy release of the prompt GRB emission ranges from 10^{48} to 10^{55} erg (Kumar & Zhang 2015), making GRBs the most energetic stellar explosions in our universe. In the era of BeppoSAX (Fishman & Meegan 1995), multi-wavelength (from X-ray to radio) afterglows following the prompt emission were detected, which help to localize GRBs precisely. The first redshift measurement was made for GRB 970508 (Metzger et al. 1997). Its spectrum revealed a redshift of 0.835, which formally confirms its cosmological origin. GRBs can even be observed up to $z \sim 10$ with current detectors (Cucchiara et al. 2011). After decades of observations and researches, people have obtained a general picture of GRB physics. The widely accepted model to explain the origin of GRBs is the so called "fireball" model (Rees & Meszaros 1992; Piran et al. 1993; Wijers et al. 1997; Mészáros 2006). The prompt emission is considered to be produced by internal shocks due to the interaction of ejecta in the fireball,

Corresponding author: Yong-Feng Huang
hyf@nju.edu.cn, gengjinjun@nju.edu.cn

[1] Some ultra-long GRBs even last for tens of thousands of seconds (Levan et al. 2014).

while the broadband afterglow is produced by the interaction between the GRB ejecta and the circumburst medium (Mészáros & Rees 1997; Vietri 1997; Tavani 1997; Waxman 1997; Sari 1997; Huang et al. 1999, 2000).

It has long been found that GRBs can be grouped into two distinct classes by considering their durations and spectral hardness (Kouveliotou et al. 1993; Bromberg et al. 2013). Long GRBs typically last for 20 – 30 s, while short GRBs typically last for 0.2 – 0.3 s. Besides, short GRBs are on average harder than long GRBs in hardness ratio. Long GRBs, with a good number being identified to be associated with core-collapse supernovae (Galama et al. 1998; Hjorth et al. 2003; Stanek et al. 2003; Campana et al. 2006; Xu et al. 2013), are generally believed to originate from the deaths of massive stars. In contrast, the favored scenario for short GRBs is the coalescence of two compact stars, especially two neutron stars (Paczynski 1986; Eichler et al. 1989, NS-NS), or a neutron star and a black hole (Paczynski 1991, NS-BH). In both the collapsar models and the coalescence models, the violent explosion would generate a stellar-size, hyper-accreting black hole, or a rapidly-spinning, strongly-magnetized neutron star (Usov 1992; Thompson 1994; Dai & Lu 1998; Popham et al. 1999; Rosswog et al. 2003; Lei et al. 2013). Recently, the detection of gravitational waves with the advanced Laser Interferometer Gravitational Wave Observatory (LIGO) opened a "multi-messenger" era in astronomy studies(Abbott et al. 2016a,b, 2017a,b). The association of the gravitational wave event GW170817 and the short event of GRB 170817A confirms the binary neutron star coalescence scenario for short GRBs (Abbott et al. 2017a; Goldstein et al. 2017).

Although important progresses have been made toward understanding GRBs, some crucial issues still remain unsolved. With a cosmological origin, GRBs could be used as a powerful tool to probe the early universe. Nevertheless, compared to type Ia supernovae (SNe Ia), GRBs are not perfect standard candles. The luminosities of GRBs cover several orders of magnitude. Their diversity, together with the complex classifications and triggering mechanisms, prevents direct applications of GRBs in cosmology. Interestingly, a few correlations have been found between various GRB parameters, either on GRB prompt emission (Amati et al. 2002; Norris et al. 2000; Ghirlanda et al. 2004, 2009; Yonetoku et al. 2004; Tsutsui et al. 2009; Willingale et al. 2010; Geng & Huang 2013; Zhang et al. 2018), or on the afterglow (Liang & Zhang 2005; Oates et al. 2009, 2012; Dainotti et al. 2010, 2016, 2017; Xu & Huang 2012; Liang et al. 2015). These correlations can provide important clues for studying the physical mechanisms of the GRB central engines. They can also hopefully make GRBs as some kinds of standard candles so that these energetic events can be used to limit cosmological parameters (Fenimore & Ramirez-Ruiz 2000; Schaefer 2003, 2007; Dai 2004; Ghirlanda et al. 2004, 2006; Wang & Dai 2006; Amati et al. 2008; Wang et al. 2011, 2015). In this aspect, a lot of work still needs to be done because GRBs originate from various mechanisms.

There is a special subclass of GRBs, i.e., GRBs with a plateau phase in the X-ray light curve. They are characterized by a shallow decay phase followed by a normal decay in X-ray afterglow. The X-ray light curve of the shallow decay phase is usually very flat so that it typically shows up as a plateau, while the power-lay index of the subsequent normal decay is usually ~ -1. It is usually believed that the plateau phase is due to some kinds of extra energy injection into the external shock, possibly from a long-lasting central engine (Dai & Lu 1998; Zhang & Mészáros 2001; Rowlinson et al. 2010, 2013; Bucciantini et al. 2012; Gompertz et al. 2013; Geng et al. 2016). Thus the X-ray plateau observations can help constrain various central engine models. For example, Li et al. (2018) analyzed the *Swift*/XRT light curves of 101 GRBs that have a plateau phase (and with the redshift being available). They compared the energetics with the maximum energy budget of magnetars ($\sim 2 \times 10^{52}$ erg), trying to determine whether the central engine is a magnetar or a black hole. More interestingly, it is also found that there exists another special kind of plateau, known as the "internal plateau", characterized by a plateau followed by an extremely rapid decay (decay index usually < -3). Such a rapid decay at the end of the "internal plateau" is much steeper than that due to the evolution of the synchrotron emission from a decelerating forward shock, but has to invoke some internal dissipation processes. One promising interpretation within the magnetar framework is that the "internal plateau" is due to the continuous energy supply from a "supra-massive" neutron star. The neutron star will finally collapse into a black hole, leading to a sudden switching off of the central engine, which manifests as the subsequent steep decay phase. The collapse of the supra-massive neutron star may either be triggered by spinning down, or by fall-back accretion, e.g., GRB 070110 as studied by Chen et al. (2017) and GRB 170714A as studied by Hou et al. (2018). Comparing with the "internal plateau", a plateau followed by a normal decay is usually called an "external plateau" due to the fact that it can be well explained by the deceleration of the external shock.

Several interesting correlations are obtained for GRBs with a plateau phase. Dainotti et al. (2008) first found an anti-correlation between the end time of the plateau phase in the GRB rest frame (T_a) and the corresponding X-ray luminosity at that moment (L_X). By analyzing a sample of 77 GRBs, they derived the relation as $L_X \propto$

$T_a^{-1.06\pm0.27}$(Dainotti et al. 2010). Xu & Huang (2012, hereafter, XH2012) further found a much tighter three-parameter correlation among T_a, L_X and the isotropic energy in the prompt emission ($E_{\gamma,\rm iso}$, here we denote it as the L-T-E correlation), e.g., $L_X \propto T_a^{-0.87\pm0.09} E_{\gamma,\rm iso}^{0.88\pm0.08}$. Dainotti et al. (2017) later also presented a $L_X - T_a - L_{\gamma,\rm peak}$ correlation between T_a, L_X, and the peak luminosity in the prompt emission ($L_{\gamma,\rm peak}$), $L_X \propto T_a^{-0.83\pm0.10} L_{\rm peak}^{0.64\pm0.11}$. Interestingly, Si et al. (2018) recently analyzed 50 GRBs which have a plateau phase in the optical afterglow light curve. They also found a similar three-parameter correlation for their sample. Their analysis indicates $L_{b,z} \propto T_{b,z}^{-0.9} E_{\gamma,\rm iso}^{0.4}$ and $L_{b,z} \propto T_{b,z}^{-0.9} E_{\rm p,i}^{0.5}$, where $T_{b,z}$ is the break time of the plateau phase in the optical band, $L_{b,z}$ is the corresponding optical luminosity during the plateau phase, and $E_{\rm p,i}$ is the peak energy of the prompt emission. For a comprehensive overview of various GRB correlations, one may refer to Wang et al. (2019), or Zhao et al. (2019).

In this study, we have collected a sample of 174 *Swift* GRBs that have a plateau phase in the X-ray afterglow light curve. These GRBs, all with the redshift being measured, occurred between March 2005 and August 2018. This sample provides a good opportunity for various statistical analysis. We fit the light curve of each GRB to get relevant parameters of the plateau phase, and then explore potential correlations between various pairs of parameters. Especially, the L-T-E correlation is extensively examined with this enlarged sample, and the physics behind the L-T-E correlation is investigated. The structure of our article is organized as follows. We describe the sample selection and data reduction processes in Section 2. The data are statistically analyzed and the results are presented in Section 3. In Section 4, we briefly summarize our conclusions and discuss the implications.

2. SAMPLE SELECTION AND DATA ANALYSIS

After the successful launch of *Swift* in 2004 (Gehrels et al. 2004), many interesting features were soon discovered in the X-ray afterglows of some GRBs, including X-ray flares and the plateau phase (Zhang et al. 2006; Nousek et al. 2006). In this paper, we mainly analyze *Swift* GRBs with a plateau phase in the X-ray light curve. Our sample are selected from the GRBs occurred between March 2005 and August 2018, all with the redshift being measured. The observed X-ray data are taken from the *Swift* GRB light curve repository (Evans et al. 2007, 2009), with the spectrum range of the light curve being 0.3 — 10 keV. We select our GRBs by the following four criteria: (1) There should be an obvious flat segment in the X-ray light curve that could be reliably identified as a plateau phase. To be more specific, we require that the power-law index of the plateau phase should be in a range of -1.0 — $+1.0$. We exclude any GRBs that do not meet this requirement. (2) There are abundant observational data points during the plateau phase. This is to ensure that the light curve can be well defined during the fitting process so that we could correctly extract the key parameters relevant to the plateau phase without any difficulties. (3) There are no flares observed during the plateau phase. Again it is to ensure a smooth fit of the plateau phase. (4) The redshift should be available for the event, so that we could calculate the isotropic γ-ray energy release ($E_{\gamma,\rm iso}$). Also, with the redshift, we will be able to derive the intrinsic T_a parameter by considering the time dilation effect. With these four criteria, we finally obtained a sample of 174 GRBs. The redshift range of our sample is 0.04 — 8.0. We note that seven short GRBs ($T_{90} < 2$ s) are interestingly included in this sample, as listed in Table 1.

Table 1. Seven Short GRBs Included in Our Sample

GRB name	T_{90} (s)	z
GRB 051221A	1.4	0.55
GRB 061201	0.76	0.11
GRB 070809	1.3	0.22
GRB 090510	0.3	0.90
GRB 130603B	0.18	0.36
GRB 140903A	0.3	0.35
GRB 150423A	0.22	1.40

Having selected the sample, we then fit the X-ray light curve of each GRB with a smoothly broken power-law function, which takes the form of (Evans et al. 2009; Li et al. 2012; Yi et al. 2016)

$$F_X(t) = F_{X0}\left[\left(\frac{t}{T_0}\right)^{\alpha_1\omega} + \left(\frac{t}{T_0}\right)^{\alpha_2\omega}\right]^{-1/\omega}. \quad (1)$$

Here, α_1 is the power-law index during the plateau phase, which should generally be close to zero. α_2 describes the decay in the following phase. T_0 is the observed end time of the plateau phase. The end time in the GRB rest frame can then be obtained by $T_a = T_0/(1+z)$. $F_{X0} \times 2^{-1/\omega}$ is the corresponding flux at the end of the plateau, and ω is a smoothness parameter, characterizing the sharpness of the transition from the plateau phase to the subsequent decay phase.

Fitting the observed X-ray light curves of the GRBs in our sample with Equation (1), we can get the main parameters relevant to the plateau phase, i.e., the end time of the plateau phase (T_a), the flux at the break time (F_{X0}), the power-law timing index during the plateau phase (α_1), and the power-law timing index in the following decaying phase (α_2). In order to get the best fit, the Markov chain Monte Carlo (MCMC) algorithm is applied. 10^6 samples are generated to fit the light curves.

Our best fit results for the X-ray light curves of all the 174 GRBs are presented in Figure 1, which can give us a general idea on what the plateau is like and how good the fit is. We obtain α_1, α_2, T_a and F_{X0} of all GRBs in our sample after the light curve fittings. The range of α_1 is (-0.79, 0.79), and the range of α_2 is (0.80, 15.11). It is interesting to note that several GRBs have very large α_2 values, which means their plateau phase is followed by a very steep decay. In other words, the plateau phase in these GRBs should be "internal plateau". Here we use a quantified criteria of $\alpha_2 > 2 + \beta_X$ to define "internal plateaus", where the convention of $F_\nu \propto t^{-\alpha}\nu^{-\beta_X}$ is used and β_X corresponds to the spectral index of the X-ray afterglow (Evans et al. 2009). According to this criteria, 11 GRBs in our sample have "internal plateaus", which are listed in Table 2.

Table 2. GRBs with an"Internal Plateau" in Our Sample

GRB name	α_2	z
GRB 050730	2.77	3.97
GRB 060607A	3.47	3.08
GRB 070110	8.95	2.35
GRB 100219A	4.64	4.7
GRB 100902A	4.69	4.5
GRB 111209A	15.11	0.68
GRB 111229A	3.15	1.38
GRB 120521C	3.03	6.0
GRB 120712A	3.26	4.17
GRB 130408A	3.79	3.76
GRB 170714A	4.97	0.79

Our sample is one of the largest sample of GRBs with a plateau phase so far. The number of GRBs in our sample is about three times that of XH2012, which only includes 55 "golden" events. Comparing with XH2012's study, we have removed several GRBs from XH2012 sample because they do not meet the selection criteria applied here, e.g. GRBs 050724 and 070802. Li et al. (2018) recently composed a sample of 101 *Swift* GRBs (up to 2017 May), which seems to be quite incomplete as compared with our sample. It is interesting to note that the sample of Dainotti et al. (2017) includes 183 GRBs with X-ray plateaus (up to 2016 August). However, in their selection process, they did not impose any compulsory conditions to identify the plateau phase clearly. In our study, we require that the power-law timing index during the plateau phase should be in the range of -1.0 — $+1.0$. This can effectively avoid confusing those GRBs with a jet break as a GRB with a plateau phase. For those GRBs with a jet break, the timing index is usually ~ -1, then followed by a steeper decay with a slope of ~ -2). They might be confused as a GRB with a plateau phase in some cases.

With F_{X0} being derived from the fitting, the X-ray luminosity at the end time of the plateau phase (L_X) can be calculated as (Willingale et al. 2007),

$$L_X = \frac{4\pi D_{\rm L}^2(z) F_{X0}}{(1+z)^{1-\beta_X}}, \tag{2}$$

where z is the redshift and $D_{\rm L}(z)$ is the luminosity distance. The values of z and β_X are obtained from the *Swift* GRB Table[2]. Note that in the *Swift* table, two redshifts are available for GRB 151027A: XRT suggests a redshift of 0.38, while Keck and GMG give a redshift of 0.81. As noted on the website, the XRT measurement is only a tentative value. Thus we chose GRB 151027A's redshift as 0.81. Another special case is GRB 101225A, for which Keck I gives a redshift of 3.8 while Gemini GMOS gives a redshift of 0.847. In this case, we adopted the larger z value (3.8) since the smaller redshift of 0.847 may be due to absorption features of the foreground galaxies. All through this study, we take a fla t ΛCDM cosmology with $H_0 = 70.0$ km s^{-1} Mpc^{-1} and $\Omega_{\rm M} = 0.286$ to calculate $D_{\rm L}(z)$.

The observed isotropic γ-ray energy ($E'_{\gamma,\rm iso}$) of the prompt emission is calculated from

$$E'_{\gamma,\rm iso} = \frac{4\pi D_{\rm L}^2(z) S}{1+z}, \tag{3}$$

where S is the BAT fluence (15 — 150 keV, in units of erg/cm^2), also taken from the *Swift* GRB table.

The so called k-correction should be considered in our calculations. Due to the cosmological time dilation, the observer frame 15-150 keV bandpass of Swift GRBs is different from the rest-frame bandpass with redshift (Bloom et al. 2001). Considering this effect, the corrected isotropic energy should be

$$E_{\gamma,\rm iso} = E'_{\gamma,\rm iso} \times \frac{\int_{15/1+z}^{150/1+z} E\Phi(E)\,dE}{\int_{15}^{150} E\Phi(E)\,dE}, \tag{4}$$

where $\Phi(E)$ is the energy spectrum. Typically, the peak energy of the observed GRB prompt emission is $\sim$ 200 — 300 keV (Preece et al. 2000; Goldstein et al. 2012). Since Swift/BAT observations are carried out in a relatively narrow energy range (15 — 150 keV), we adopt a simple power-law spectral model, i.e., $\Phi(E) = E^{\alpha_\gamma}$, to calculate the k-correction in this study. Here α_γ is the photon spectral index, taken from the *Swift* GRB table. The derived k-corrections for the GRBs of our sample are mainly in the range of 0.07 — 1.7.

The various parameters relevant to our study are listed in Table 3, which includes the GRB name, T_{90}, redshift (z), BAT fluence (S), power-law index of the plateau phase (α_1), power-law index of the subsequent segment (α_2), the end time of the plateau phase (T_a), the corresponding luminosity at the end time (L_X), and the isotropic energy ($E_{\gamma,\rm iso}$). After getting all the relevant data, we then can explore the correlations between various parameters. The L-T-E correlation can also be thoroughly examined. We present the results in the next section.

3. RESULTS

3.1. *Parameter Distributions*

In Figure 2, we plot the distributions of L_X, T_a, and $E_{\gamma,\rm iso}$. The typical value of $L_{\rm x}$ is 2.6×10^{47} erg·s^{-1} with a 50% distribution range of (0.4, 12)$\times 10^{47}$ erg·s^{-1}. The typical value of T_a is 2.4×10^3 s with a 50% distribution range of (0.8, 7)$\times 10^3$ s. The typical value of $E_{\gamma,\rm iso}$ is 0.13×10^{53} s, with a 50% distribution range of (0.04, 0.3)$\times 10^{53}$ erg. We notice that the distributions of these three parameters are very similar to those of XH2012 sample. For XH2012 sample, the typical value of $L_{\rm x}$ is 3.9×10^{47} erg·s^{-1} with a 50% distribution range of (0.4, 17)$\times 10^{47}$ erg·s^{-1}; the typical value of T_a is 2.5×10^3 s, with a 50% distribution range of (0.9, 10)$\times 10^3$ s; and the typical value of $E_{\gamma,\rm iso}$ (bolometric isotropic energy, in XH2012) is 0.62×10^{53} erg, with a 50% distribution range of (0.07, 1.1)$\times 10^{53}$ erg.

The distributions of S, z, and T_{90} are displayed in Figure 3. The typical value of S is 20×10^{-7} erg·cm^{-2}, with a 50% distribution range of (8, 50)$\times 10^{-7}$ erg·cm^{-2}. The typical value of z is 2.0, with a 50% distribution range of (1.0, 3.2). As for T_{90}, the typical value is 58 s, with a 50% distribution range of (18, 123) s. The distribution of T_{90} indicates that most GRBs in our sample are long GRBs.

α_1 and α_2 are two important parameters derived from our light curve fitting. Although we have applied a criteria of $-1.0 \leq \alpha_1 \leq +1.0$ in selecting the GRBs with a plateau phase, α_1 actually has a typical value of 0.11 for our whole sample, with a 50% distribution range of (0.03, 0.3). It means that in most cases, the timing index of the plateau is in the range of 0.03 — 0.3, so that the plateau phase is really very flat in the light curve. Again, it supports the idea that the plateau phase is a special phenomenon in GRB afterglows. In our sample, α_2 has a typical value 1.5, with a 50% distribution range of 1.3 — 1.9 (see Figure 4). For the internal plateau sub-sample, we find that the typical

[2] https://swift.gsfc.nasa.gov/archive/grb_table.html/

value of $\alpha_{1,\rm int}$ is 0.23, with a 50% distribution range of 0.06 — 0.5; and the typical value of $\alpha_{2,\rm int}$ is 3.8, with a 50% distribution range of 3.2 — 5. We have also calculated the slope variation of $\Delta\alpha = \alpha_2 - \alpha_1$. The typical value of $\Delta\alpha$ is 1.4 for the whole sample, with a 50% distribution range of 1.1 — 1.7; and it is $\Delta\alpha_{\rm int} = 3.5$ for the internal plateau sub-sample, with a 50% distribution range of 3.0 — 4.4. We have also applied the K-S test on $\Delta\alpha$ for the internal plateau sub-sample and the rest of the whole sample. The derived p-value is as small as 5×10^{-10}, which means the internal plateau GRBs are very likely to form a distinct subclass.

3.2. *Two-Parameter Correlations*

Here, we investigate whether there are any significant correlations between various parameter pairs. In Figure 5, we plot L_X versus T_a, L_X versus $E_{\gamma,\rm iso}$, S versus T_{90}, and $E_{\gamma,\rm iso}$ versus T_{90}, respectively. It could be clearly seen that these parameter pairs are somewhat correlated. For the $L_X - T_a$ correlation, the best fit result is $\log(L_X/10^{47}{\rm erg\cdot s^{-1}}) = (0.76 \pm 0.13) + (-1.12 \pm 0.18)\log(T_a/10^3{\rm s})$, with the Spearmaan correlation coefficient $\rho = -0.74$ and a chance probability $p = 2 \times 10^{-31}$. For the $L_X - E_{\gamma,\rm iso}$ correlation, the best fit result is $\log(L_X/10^{47}{\rm erg\cdot s^{-1}}) = (1.55 \pm 0.20) + (0.97 \pm 0.13)\log(E_{\gamma,\rm iso}/10^{53}{\rm erg})$. The Spearman correlation coefficient ρ is 0.60, with a chance probability $p = 1 \times 10^{-18}$. Generally speaking, these two-parameter correlations are still quite dispersive. In the next subsection, we will see that when we use the three parameters of L_X, T_a and $E_{\gamma,\rm iso}$ to get a three-parameter correlation, it would be much tighter. We have also used the bivariate Bayesian linear regression procedure (Kelly 2007) to further check these two parameter correlations. This method can conveniently take into account the heteroscedastic measurement errors. The fitting results are $\log(L_X/10^{47}{\rm erg\cdot s^{-1}}) = (0.81 \pm 0.07) + (-1.33 \pm 0.10)\log(T_a/10^3{\rm s})$ with an intrinsic scatter of 0.59, and $\log(L_X/10^{47}{\rm erg\cdot s^{-1}}) = (1.37 \pm 0.10) + (1.01 \pm 0.07)\log(E_{\gamma,\rm iso}/10^{53}{\rm erg})$ with an intrinsic scatter of 0.64. We see that the results are consistent with the previous least square linear fits.

Additionally, we find that both S and $E_{\gamma,\rm iso}$ are positively correlated with T_{90}. The best fit results are $\log(S/10^{-7}{\rm erg\cdot cm^{-2}}) = (0.72 \pm 0.06) + (0.34 \pm 0.03)\log(T_{90}/{\rm s})$ with a Spearman correlation coefficient of $\rho = 0.54$ and a chance probability of $p = 2 \times 10^{-14}$, and $\log(E_{\gamma,\rm iso}/10^{53}{\rm erg}) = (-1.71 \pm 0.22) + (0.42 \pm 0.11)\log(T_{90}/{\rm s})$ with a Spearman correlation coefficient of $\rho = 0.55$ and a chance probability of $p = 1 \times 10^{-14}$, respectively. The Spearman correlation coefficients support the existence of the S - T_{90} and $E_{\gamma,\rm iso}$ - T_{90} correlations, but note that these correlations again are relatively dispersive. As a reference, the fitting results by using the bivariate Bayesian linear regression procedure are: $\log(S/10^{-7}{\rm erg\cdot cm^{-2}}) = (0.52 \pm 0.10) + (0.48 \pm 0.05)\log(T_{90}/{\rm s})$ with an intrinsic scatter of 0.22, and $\log(E_{\gamma,\rm iso}/10^{53}{\rm erg}) = (-2.15 \pm 0.17) + (0.67 \pm 0.10)\log(T_{90}/{\rm s})$ with an intrinsic scatter of 0.46. Note that T_{90} might be detector dependent (Bromberg et al. 2013; Resmi 2017), but this effect should not be significant in our sample, since all our bursts are *Swift* GRBs. Generally, the positive correlations of $S - T_{90}$ and $E_{\gamma,\rm iso} - T_{90}$ are not difficult to understand. It means the observed intensities of GRBs are somewhat in a limited range.

In these plots, we have also marked the 7 short GRBs in our sample with green squares, and the 11 GRBs of "internal plateaus" with red triangles, to see whether there are any systematic difference in these sub-samples. It is interesting to note that in all the four panels of Figure 5, the internal plateau sub-sample is largely consistent with the whole sample. We speculate that maybe the reason is that all the internal plateau GRBs in our sample are essentially long GRBs. In order to further investigate the nature of the internal plateau sub-sample, we have applied the Bromberg criteria test on these GRBs, following Bromberg et al. (2013). The Bromberg criteria is an improved classification method for distinguishing long GRBs (or more precisely, collapsars) and short GRBs (or non-collapsars) by considering the duration as well as the hardness. More specifically, for *Swift* GRBs, if the harness raito is hard (Power-Law index PL > -1.13), then the critical duration for long and short GRBs is $2.8^{+1.5}_{-1.0}$ s; If the harness raito is intermediate (-1.65 < PL < -1.13), then the critical duration is $0.6^{+0.2}_{-0.3}$ s; If the harness raito is soft (PL < -1.65), then the separation duration is $0.3^{+0.4}_{-0.2}$ s. In addition to T_{90} and the hardness ratio, we further calculated the probability for the GRB to be a non-collapar, i.e. the non-collapsar probability (f_{NC}) in Bromberg et al. (2013). The results are listed in Table 4. Note that for two GRBs (111209A and 170714A), the T_{90} data are unavailable so that the test cannot be applied. Table 4 clearly shows that all other "internal plateau" GRBs in our sample are long GRBs based on the Bromberg criteria test.

Contrastively, although the short GRB sub-sample is also generally consistent with the whole sample, there is still some systematic deviation. It is most significant in Figure 5(a). Maybe it is due to the fact that long GRBs and short GRBs have quite different origins.

In Figure 6, we plot our sample on the L_X - z, $E_{\gamma,\rm iso}$ - z, and T_a - z planes. Figure 6(a) and 6(b) show that GRBs at high redshifts usually have a relatively larger L_X and $E_{\gamma,\rm iso}$. This may be due to the selection effect: at a large

distance, GRBs with a small L_X and $E_{\gamma,\rm iso}$ will generally be too weak to be observed, since our detectors have a limited threshold. In Figure 6(a), we have plotted the XRT detection limit with the dashed line, which corresponds to a minimum flux of $f_{\rm lim} \sim 2\times10^{-14}$ erg cm^{-2} s^{-1}. Note that all the observed data points are reasonably above the line. Similarly, in Figure 6(b), the dashed line represents the BAT detection limit for $f_{\rm lim} \sim 10^{-8}$ erg cm^{-2} s^{-1} by assuming a typical duration of 2 s. Again, all the observed data points are above the limit line.

In Figure 6c, we see that no correlation exists between T_a and z. It means that the plateau phase is somewhat redshift-independent. This tendency is especially clear for the internal plateau sub-sample.

In Figure 7, we plot our sample on a few other parameter planes. We have applied the Kendell's tau method to do the non-parametric test for any potential correlations between the parameters (see Table 5 for numerical results). The τ statistics are all rather small, indicating that there is no significant correlation between any two of the parameters.

3.3. *L-T-E Correlation*

In this section, we examine whether the L-T-E correlation still exists for our significantly expanded sample. Using the fitted T_a, L_X and $E_{\gamma,\rm iso}$ data, we fit the possible L-T-E correlation by the following expression (XH2012):

$$\log(L_X/10^{47}{\rm erg\cdot s^{-1}}) = a + b\log(T_a/10^3{\rm s}) + c\log(E_{\gamma,\rm iso}/10^{53}{\rm erg}), \tag{5}$$

where the coefficients a, b, and c are constants to be determined.

In order to get the best fit, a Markov chain Monte Carlo (MCMC) algorithm is used. 10^7 samples are generated to fit the L-T-E correlation. During our fitting, the joint likelihood function for a, b, and c is (D'Agostini 2005):

$$\mathscr{L}(a,b,c,\sigma_{\rm int}) \propto \prod_i \frac{\exp\left[-(y_i - a - bx_{1,i} - cx_{2,i})^2/(2(\sigma_{\rm int}^2 + \sigma_{y_i}^2 + b^2\sigma_{x_{1,i}}^2 + c^2\sigma_{x_{2,i}}^2))\right]}{\sqrt{\sigma_{\rm int}^2 + \sigma_{y_i}^2 + b^2\sigma_{x_{1,i}}^2 + c^2\sigma_{x_{2,i}}^2}}, \tag{6}$$

where i is the corresponding serial number of GRBs in our sample, $\sigma_{\rm int}$ represents the intrinsic scattering. Here, $x_1 = \log(L_X/10^{47}{\rm erg\cdot s^{-1}})$, $x_2 = \log(E_{\gamma,\rm iso}/10^{53}{\rm erg})$ and $y = \log(T_a/10^3{\rm s})$. $\sigma_{x_{1,i}}, \sigma_{x_{2,i}}$, and σ_{y_i} are errors of x_1, x_2, and y respectively.

We have performed the three-parameter fitting for all the 174 GRBs in our sample. The best fit result is

$$\log(L_X/10^{47}{\rm erg\cdot s^{-1}}) = (1.11\pm0.04) + (-1.01\pm0.05)\log(T_a/10^3{\rm s}) + (0.84\pm0.04)\log(E_{\gamma,\rm iso}/10^{53}{\rm erg}). \tag{7}$$

The Spearman correlation coefficient is $\rho = 0.90$, with a chance probability of $p = 2\times10^{-67}$. Our fitting result is illustrated in Figure 8, where the Y-axis is the X-ray luminosity at the end time of the plateau phase (L_X, in units of 10^{47} erg/s), and the X-axis is a combination of T_a (in units of 10^3 s) and $E_{\gamma,\rm iso}$ (in units of 10^{53} erg). We see that the observed data points are distributed tightly along the best fit line.

Comparing with the two-parameter correlations presented in the above subsection, such as the L_X - T_a correlation ($L_X \propto T_a^{-1.10\pm0.20}$, see Figure 5a) and the L_X - $E_{\gamma,\rm iso}$ correlation ($L_X \propto E_{\gamma,\rm iso}^{0.97\pm0.13}$, see Figure 5b), the L-T-E correlation is much tighter. The correlation coefficient is very close to 1. The error bars of the parameters derived here are also much smaller, with the intrinsic scatter of the L-T-E correlation being as small as $\sigma_{\rm int} = 0.39\pm0.03$.

Our result indicates that $L_X \propto T_a^{-1.01\pm0.05}E_{\gamma,\rm iso}^{0.84\pm0.04}$. The relation is generally consistent with the result of XH2012, which reads $L_X \propto T_a^{-0.87\pm0.09}E_{\gamma,\rm iso}^{0.88\pm0.08}$. The error bars of our derived indices are roughly one half of those in XH2012, showing that the correlation is even tighter here. It is striking to see that the L-T-E correlation still exists for such a significantly enlarged sample, with an even smaller dispersion.

Several different models have been suggested to interpret the plateau phase. First, it may be due to a structured jet. In this case, emission from the high latitude ejecta will peak at a later stage as compared with the central energetic ejecta, leading to a slower decay of the afterglow. Second, it may be produced by a stratified fireball. In this case, the material in different shells have different velocities. Slower shells will finally catch up with the preceding faster shells and supply energy into the external shock to show up as the plateau phase. Generally, in the above two kinds of models, some arbitrary assumptions have to be made to depict the jet structure or the velocity distribution of the ejecta, and no simple conclusions could be drawn for the plateau phase.

In a third model, it is argued that the plateau phase is produced by energy injection from a rapidly spinning millisecond magnetar that resides at the center of the GRB remnant (Zhang & Mészáros 2001; Dai 2004; Troja et al. 2007; Dall'Osso et al. 2011; Metzger et al. 2011; Rowlinson et al. 2013, 2014; Siegel et al. 2014; Yi et al. 2014; Rea

et al. 2015; Lü et al. 2018). In this model, after the prompt burst, the millisecond magnetar loses its rotational energy due to spinning down, generating a Poynting-flux or an electron-positron wind and injecting energy into the external shock. Xu & Huang (2012) suggested that the L-T-E correlation supports this magnetar model. It has been shown that the luminosity of the energy injection is roughly constant within the characteristic spinning down time of the magnetar (Dai 2004), naturally leading to a plateau phase. After the magnetar spins down, the energy injection ceases. So, Xu & Huang argued that the product of the observed L_X and T_a gives a good measure for the rotational energy of the magnetar. On the other hand, the isotropic γ-ray energy release ($E_{\gamma,\rm iso}$) is also closely related to the rotational energy. As a result, we roughly have $L_X \times T_a \propto E_{\gamma,\rm iso}$, i.e., $L_X \propto E_{\gamma,\rm iso} {T_a}^{-1}$. It is interesting to note that our fitting result of $L_X \propto T_a^{-1.01\pm0.05} E_{\gamma,\rm iso}^{0.84\pm0.04}$ is again consistent with the theoretical expectation. The fitted power-law index of T_a is -1.01 ± 0.05, very close to -1, and the fitted power-law index of $E_{\gamma,\rm iso}$ is 0.84 ± 0.04, also close to 1. We thus suggest that our updated L-T-E correlation is a support for the magnetar explanation of the X-ray plateaus.

In Figure 8, we have marked the short GRB sub-sample (7 events) with green squares. Interestingly, these short GRBs follow the same L-T-E correlation. They are generally at the low luminosity end of the plot, but they are distributed along the best fit line almost as tightly as other GRBs. Theoretically, while a millisecond magnetar may be born during the hypernova that gives birth to a long GRB (Usov 1992; Bucciantini et al. 2009; Metzger et al. 2011), it has also been argued that the central engine of short GRBs could also be magnetars (Dai et al. 2006; Fan & Xu 2006; Metzger et al. 2008; Kiuchi et al. 2012; Lü et al. 2015). The distribution of the short GRB sub-sample on Figure 8 suggests that the leftover of the double compact star merger might be a magnetar in these cases.

In Figure 8, we have also specially marked the "internal plateau" sub-sample (11 GRBs) with red triangles. As mentioned before, for these internal plateau GRBs, the most popular explanation is that a fast-rotating supra-massive neutron star is initially born associated with the GRB. It then collapses into a black hole after significantly spinning down. So, the internal plateau sub-sample are valuable events for checking our magnetar explanation of the plateau phase. In Figure 8, we see that these GRBs do follow the same L-T-E correlation as expected. However, we also note that the scattering of the red triangles are slightly larger than other data points. It may be due to the fact that the condition that determines the end time of the internal plateau phase is somewhat different from other GRBs. For normal plateaus, the end time is reached when the magnetar loses half of its rotational energy, while for internal plateaus, the end time is achieved when the magnetar rotates slowly enough so that it cannot resist the gravity. So, in the internal plateau case, the end time is dependent on both the initial spinning period and the initial mass.

4. DISCUSSION

In this study, we focus on those GRBs with a plateau phase in the X-ray afterglow light curve. We define the plateau phase by requiring that the power-law timing index should be in a range of -1.0 — $+1.0$. We finally extracted a large sample of 174 events from the *Swift* GRBs that happened between March 2005 and August 2018, all with the redshift being measured. Statistical analysis is then carried out based on the sample. It is found that some parameter pairs are more or less correlated, such as L_X vs. T_a, L_X vs. $E_{\gamma,\rm iso}$, S vs. T_{90}, and $E_{\gamma,\rm iso}$ vs. T_{90}. However, the most striking finding about our sample is that the three-parameter L-T-E correlation still exists when the capacity of our sample has been significantly expanded as compared with that of XH2012. The best fitting result gives $L_X \propto T_a^{-1.01} E_{\gamma,\rm iso}^{0.84}$, also largely consistent with the result of XH2012. It is argued that the L-T-E correlation supports the magnetar explanation for the plateau phase. In our study, two sub-samples have been identified, i.e. short GRBs with a plateau phase and those GRBs with a so called "internal plateau". It is interesting to note that the same L-T-E correlation is followed by these two sub-samples, indicating that a rapidly rotating millisecond magnetar might have been born during the GRB.

Short GRBs are generally believed to be produced by the merger of binary compact stars, such as by a double neutron star system or by a black hole-neutron star binary. For the merger of a black hole and a neutron star, the aftermath is undoubtedly a black hole. However, for the merger of a double neutron star system, the case is much more complicated. The leftover could be either a black hole or a massive neutron star. Here, for the short GRBs with an X-ray plateau as in our sample, the L-T-E correlation strongly indicates that the leftover of the merger should be a neutron star that has a strong magnetic field and spins at millisecond period. However, we should also notice that only a small fraction of short GRBs has the plateau phase. For other short GRBs, we cannot accurately determine the aftermath of the merger. Anyway, the merit of our study is that it proves that at least some of the short GRBs are produced by double neutron star mergers, and that a fraction of them lead to the birth of massive millisecond magnetars.

For GRBs that have an internal plateau, the most natural interpretation is that a rapidly rotating supra-massive magnetar is born at the center. The plateau phase is then followed by a steep decay when the magnetar collapse to form a black hole after it spins down significantly so that it cannot resist the gravity. As a result, it is naturally expected that internal plateau GRBs should also follow the L-T-E correlation, as shown in Figure 8. Though some authors recently have suggested that it is possible to explain the internal plateaus by some other mechanisms such as the deceleration of the ejecta by external medium (Beniamini & Mochkovitch 2017; Beniamini et al. 2017; Metzger et al. 2018), our results support the magnetar interpretation of the L-T-E correlation.

In our study, the sub-sample of short GRBs is consisted of 7 events while the sub-sample of internal plateau GRBs is consisted of 11 events. Interestingly, we find no overlapping between these two sub-samples. In other words, no internal plateau has been found in a short GRB in our sample. However, we notice that internal plateaus attributed to neutron star collapse actually have been claimed to exist in short GRBs at least by Rowlinson et al. (2013). In their study, by defining internal plateaus as $\alpha_2 > \beta_X + 2$, four short GRBs were found to have internal plateaus, e.g. GRBs 060801, 080919, 100702A, and 120305A. The former three GRBs are even listed in the *Swift* short GRB cataloge in Bromberg et al. (2013). But nearly 80% of the short GRBs in Rowlinson et al. (2013) are lacking of redshift measurements. Unfortunately, redshifts are not available for the four "internal plateau" GRBs listed above, thus they are not included in our sample. In fact, theoretically, it is more likely that the merger events would result in a supra-massive NS than the core collapse process. Before the final merge, the binary neutron stars rotate around each other at a speed close to the Kepler limit. This makes the merger remnant more likely to have greater rotational energy to generate a supra-massive NS than the core collapse. It will then result in a delayed collapse to form a black hole, and thus lead to an internal plateau. Indeed, evidence supporting the existence of supra-massive NSs after NS - NS mergers has been suggested by a few authors (Lasky et al. 2014; Lü et al. 2015; Gao et al. 2016; Li et al. 2016). In our sample, the total number of internal plateau GRBs is still very small. We cannot exclude the possibility that short GRBs may also have internal plateaus. In the future, if short GRBs with clear internal plateaus are observed and if redshifts are also measured, then the L-T-E correlation will be a useful tool to probe their nature, and the correlation itself will also be meaningfully examined.

Finally, it should be noted that in recent years, some authors have suggested that the central engine of GRBs with a plateau phase may also be newly formed black holes with a neutrino-cooling-dominated accretion flow (NDAF) (Cannizzo & Gehrels 2009; Cannizzo et al. 2011; Lü & Zhang 2014; Lei et al. 2017). Two popular mechanisms are considered to launch a continuous jet to supply energy into the external shock and produce the plateau. One is the Blandford-Znajek (BZ) mechanism, which extracts the rotational energy from a Kerr black hole (Blandford & Znajek 1977). The other is the neutrino-antineutrino annihilation mechanism, releasing gravitational energy from the accretion disk (Popham et al. 1999; Di Matteo et al. 2002; Gu et al. 2006; Liu et al. 2007; Chen & Beloborodov 2007; Janiuk et al. 2007; Lei et al. 2009; Liu et al. 2015). In reality, it is quite possible that both black holes and magnetars can somewhat act as the central engine of energy injection. Actually, Li et al. (2018) even argued that about 20% of the central engines are magnetars, and others are black holes. A mixed origin of the plateau phase may make the L-T-E correlation complicated and dispersive.

We thank the anonymous referee for valuable suggestions. This study is partially supported by the National Natural Science Foundation of China (Grants No. 11873030, and 11833003), and by the Strategic Priority Research Program of the Chinese Academy of Sciences "Multi-waveband Gravitational Wave Universe" (Grant No. XDB23040400). ZBZ acknowledges the support from two Chinese Provincial Natural Science Foundations (Grant No. 20171125 and 20165660). This work made use of data supplied by the UK *Swift* Science Data Center at the University of Leicester.

REFERENCES

Abbott, B. P., Abbott, R., Abbott, T. D., et al. 2016a, PhRvL, 116, 241103

—. 2016b, ApJS, 225, 8

—. 2017a, ApJL, 848, L13

—. 2017b, PhRvL, 118, 221101

Amati, L., Guidorzi, C., Frontera, F., et al. 2008, MNRAS, 391, 577

Amati, L., Frontera, F., Tavani, M., et al. 2002, A&A, 390, 81

Band, D., Matteson, J., Ford, L., et al. 1993, ApJ, 413, 281

Beniamini, P., Giannios, D., & Metzger, B. D. 2017, MNRAS, 472, 3058
Beniamini, P., & Mochkovitch, R. 2017, A&A, 605, A60
Blandford, R. D., & Znajek, R. L. 1977, MNRAS, 179, 433
Bloom, J. S., Frail, D. A., & Sari, R. 2001, AJ, 121, 2879
Bromberg, O., Nakar, E., Piran, T., & Sari, R. 2013, ApJ, 764, 179
Bucciantini, N., Metzger, B. D., Thompson, T. A., & Quataert, E. 2012, MNRAS, 419, 1537
Bucciantini, N., Quataert, E., Metzger, B. D., et al. 2009, MNRAS, 396, 2038
Campana, S., Mangano, V., Blustin, A. J., et al. 2006, Nature, 442, 1008
Cannizzo, J. K., & Gehrels, N. 2009, ApJ, 700, 1047
Cannizzo, J. K., Troja, E., & Gehrels, N. 2011, ApJ, 734, 35
Chen, W., Xie, W., Lei, W. H., et al. 2017, ApJ, 849, 119
Chen, W. X., & Beloborodov, A. M. 2007, ApJ, 657, 383
Cucchiara, A., Levan, A. J., Fox, D. B., et al. 2011, ApJ, 736, 7
D'Agostini, G. 2005, arXiv e-prints, arXiv:0511182
Dai, Z. G. 2004, ApJ, 606, 1000
Dai, Z. G., & Lu, T. 1998, A&A, 333, L87
Dai, Z. G., Wang, X. Y., Wu, X. F., & Zhang, B. 2006, Science, 311, 1127
Dainotti, M. G., Cardone, V. F., & Capozziello, S. 2008, MNRAS, 391, L79
Dainotti, M. G., Hernandez, X., Postnikov, S., et al. 2017, ApJ, 848, 88
Dainotti, M. G., Postnikov, S., Hernandez, X., & Ostrowski, M. 2016, ApJL, 825, L20
Dainotti, M. G., Willingale, R., Capozziello, S., Fabrizio Cardone, V., & Ostrowski, M. 2010, ApJL, 722, L215
Dall'Osso, S., Stratta, G., Guetta, D., et al. 2011, A&A, 526, A121
Di Matteo, T., Perna, R., & Narayan, R. 2002, ApJ, 579, 706
Eichler, D., Livio, M., Piran, T., & Schramm, D. N. 1989, Nature, 340, 126
Evans, P. A., Beardmore, A. P., Page, K. L., et al. 2007, A&A, 469, 379
—. 2009, MNRAS, 397, 1177
Fan, Y.-Z., & Xu, D. 2006, MNRAS, 372, L19
Fenimore, E. E., & Ramirez-Ruiz, E. 2000, arXiv e-prints, arXiv:0004176
Fishman, G. J., & Meegan, C. A. 1995, ARA&A, 33, 415
Galama, T. J., Vreeswijk, P. M., van Paradijs, J., et al. 1998, Nature, 395, 670
Gao, H., Zhang, B., & Lü, H.-J. 2016, PhRvD, 93, 044065
Gehrels, N., Chincarini, G., Giommi, P., et al. 2004, ApJ, 611, 1005
Geng, J. J., & Huang, Y. F. 2013, ApJ, 764, 75
Geng, J. J., Wu, X. F., Huang, Y. F., Li, L., & Dai, Z. G. 2016, ApJ, 825, 107
Ghirlanda, G., Ghisellini, G., & Firmani, C. 2006, NJPh, 8, 123
Ghirlanda, G., Ghisellini, G., & Lazzati, D. 2004, ApJ, 616, 331
Ghirlanda, G., Nava, L., Ghisellini, G., Celotti, A., & Firmani, C. 2009, A&A, 496, 585
Goldstein, A., Burgess, J. M., Preece, R. D., et al. 2012, ApJS, 199, 19
Goldstein, A., Veres, P., Burns, E., et al. 2017, ApJL, 848, L14
Gompertz, B. P., O'Brien, P. T., Wynn, G. A., & Rowlinson, A. 2013, MNRAS, 431, 1745
Gu, W. M., Liu, T., & Lu, J. F. 2006, ApJL, 643, L87
Hjorth, J., Sollerman, J., Møller, P., et al. 2003, Nature, 423, 847
Hou, S. J., Liu, T., Xu, R. X., et al. 2018, ApJ, 854, 104
Huang, Y. F., Dai, Z. G., & Lu, T. 1999, MNRAS, 309, 513
Huang, Y. F., Gou, L. J., Dai, Z. G., & Lu, T. 2000, ApJ, 543, 90
Janiuk, A., Yuan, Y., Perna, R., & Di Matteo, T. 2007, ApJ, 664, 1011
Kelly, B. C. 2007, ApJ, 665, 1489
Kiuchi, K., Kyutoku, K., & Shibata, M. 2012, PhRvD, 86, 064008
Kouveliotou, C., Meegan, C. A., Fishman, G. J., et al. 1993, ApJL, 413, L101
Kumar, P., & Zhang, B. 2015, PhR, 561, 1
Lasky, P. D., Haskell, B., Ravi, V., Howell, E. J., & Coward, D. M. 2014, PhRvD, 89, 047302
Lei, W. H., Wang, D. X., Zhang, L., et al. 2009, ApJ, 700, 1970
Lei, W.-H., Zhang, B., & Liang, E.-W. 2013, ApJ, 765, 125
Lei, W. H., Zhang, B., Wu, X. F., & Liang, E. W. 2017, ApJ, 849, 47
Levan, A. J., Tanvir, N. R., Starling, R. L. C., et al. 2014, ApJ, 781, 13
Li, A., Zhang, B., Zhang, N.-B., et al. 2016, PhRvD, 94, 083010
Li, L., Wu, X. F., Lei, W. H., et al. 2018, ApJS, 236, 26
Li, L., Liang, E. W., Tang, Q. W., et al. 2012, ApJ, 758, 27
Liang, E., & Zhang, B. 2005, ApJ, 633, 611
Liang, E. W., Lin, T. T., Lü, J., et al. 2015, ApJ, 813, 116
Liu, T., Gu, W.-M., Xue, L., & Lu, J.-F. 2007, ApJ, 661, 1025
Liu, T., Hou, S. J., Xue, L., & Gu, W. M. 2015, ApJS, 218, 12
Lü, H. J., & Zhang, B. 2014, ApJ, 785, 74

Lü, H. J., Zhang, B., Lei, W. H., Li, Y., & Lasky, P. D. 2015, ApJ, 805, 89
Lü, H. J., Zou, L., Lan, L., & Liang, E. W. 2018, MNRAS, 480, 4402
Meegan, C. A., Fishman, G. J., Wilson, R. B., et al. 1992, Nature, 355, 143
Mészáros, P. 2006, RPPh, 69, 2259
Mészáros, P., & Rees, M. J. 1997, ApJ, 476, 232
Metzger, B. D., Beniamini, P., & Giannios, D. 2018, ApJ, 857, 95
Metzger, B. D., Giannios, D., Thompson, T. A., Bucciantini, N., & Quataert, E. 2011, MNRAS, 413, 2031
Metzger, B. D., Quataert, E., & Thompson, T. A. 2008, MNRAS, 385, 1455
Metzger, M. R., Djorgovski, S. G., Kulkarni, S. R., et al. 1997, Nature, 387, 878
Norris, J. P., Marani, G. F., & Bonnell, J. T. 2000, ApJ, 534, 248
Nousek, J. A., Kouveliotou, C., Grupe, D., et al. 2006, ApJ, 642, 389
Oates, S. R., Page, M. J., De Pasquale, M., et al. 2012, MNRAS, 426, L86
Oates, S. R., Page, M. J., Schady, P., et al. 2009, MNRAS, 395, 490
Paczynski, B. 1986, ApJL, 308, L43
—. 1991, AcA, 41, 257
Piran, T., Shemi, A., & Narayan, R. 1993, MNRAS, 263, 861
Popham, R., Woosley, S. E., & Fryer, C. 1999, ApJ, 518, 356
Preece, R. D., Briggs, M. S., Mallozzi, R. S., et al. 2000, ApJS, 126, 19
Rea, N., Gullón, M., Pons, J. A., et al. 2015, ApJ, 813, 92
Rees, M. J., & Meszaros, P. 1992, MNRAS, 258, 41P
Resmi, L. 2017, JAA, 38, 56
Rosswog, S., Ramirez-Ruiz, E., & Davies, M. B. 2003, MNRAS, 345, 1077
Rowlinson, A., Gompertz, B. P., Dainotti, M., et al. 2014, MNRAS, 443, 1779
Rowlinson, A., O'Brien, P. T., Metzger, B. D., Tanvir, N. R., & Levan, A. J. 2013, MNRAS, 430, 1061
Rowlinson, A., O'Brien, P. T., Tanvir, N. R., et al. 2010, MNRAS, 409, 531
Sari, R. 1997, ApJL, 489, L37
Schaefer, B. E. 2003, ApJL, 583, L67
—. 2007, ApJ, 660, 16
Si, S. K., Qi, Y. Q., Xue, F. X., et al. 2018, ApJ, 863, 50
Siegel, D. M., Ciolfi, R., & Rezzolla, L. 2014, ApJL, 785, L6
Stanek, K. Z., Matheson, T., Garnavich, P. M., et al. 2003, ApJL, 591, L17
Tavani, M. 1997, ApJL, 483, L87
Thompson, C. 1994, MNRAS, 270, 480
Troja, E., Cusumano, G., O'Brien, P. T., et al. 2007, ApJ, 665, 599
Tsutsui, R., Nakamura, T., Yonetoku, D., et al. 2009, JCAP, 8, 015
Usov, V. V. 1992, Nature, 357, 472
Vietri, M. 1997, ApJL, 488, L105
Wang, F., Zou, Y. C., Liu, F., et al. 2019, arXiv e-prints, arXiv:1902.05489
Wang, F. Y., & Dai, Z. G. 2006, MNRAS, 368, 371
Wang, F. Y., Dai, Z. G., & Liang, E. W. 2015, NewAR, 67, 1
Wang, F. Y., Qi, S., & Dai, Z. G. 2011, MNRAS, 415, 3423
Waxman, E. 1997, ApJL, 485, L5
Wijers, R. A. M. J., Rees, M. J., & Meszaros, P. 1997, MNRAS, 288, L51
Willingale, R., Genet, F., Granot, J., & O'Brien, P. T. 2010, MNRAS, 403, 1296
Willingale, R., O'Brien, P. T., Osborne, J. P., et al. 2007, ApJ, 662, 1093
Xu, D., de Ugarte Postigo, A., Leloudas, G., et al. 2013, ApJ, 776, 98
Xu, M., & Huang, Y. F. 2012, A&A, 538, A134 (XH2012)
Yi, S. X., Dai, Z. G., Wu, X. F., & Wang, F. Y. 2014, arXiv e-prints, arXiv:1401.1601
Yi, S. X., Xi, S. Q., Yu, H., et al. 2016, ApJS, 224, 20
Yonetoku, D., Murakami, T., Nakamura, T., et al. 2004, ApJ, 609, 935
Zhang, B., Fan, Y. Z., Dyks, J., et al. 2006, ApJ, 642, 354
Zhang, B., & Mészáros, P. 2001, ApJL, 552, L35
Zhang, Z. B., Zhang, C. T., Zhao, Y. X., et al. 2018, PASP, 130, 054202
Zhao, L., Zhang, B., Gao, H., et al. 2019, arXiv e-prints, arXiv:1908.01561

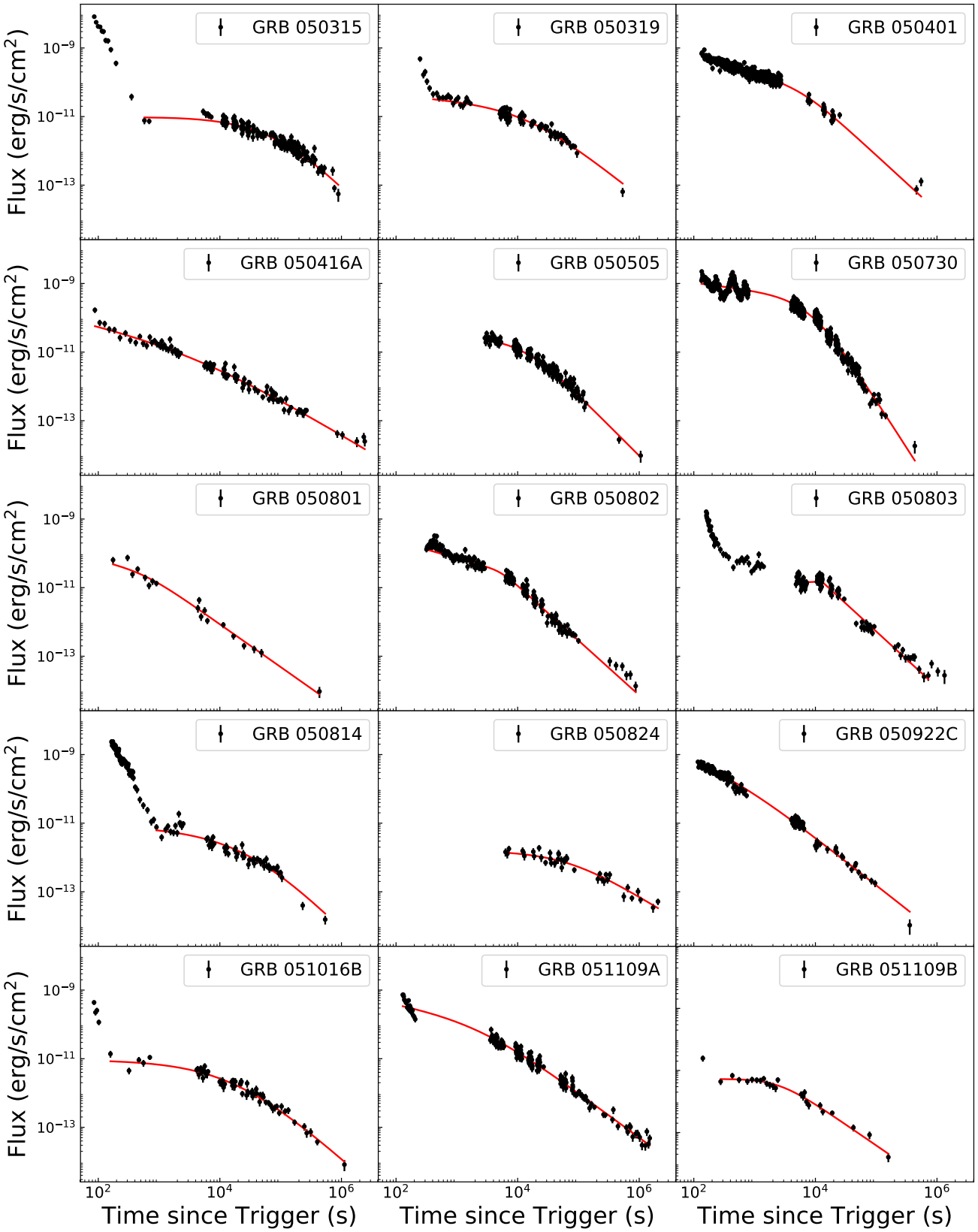

Figure 1. Observed X-ray afterglows of all the 174 GRBs in our sample, and our best fit to the light curves. Black dots correspond to the observational data by *Swift*/XRT (Evans et al. 2007, 2009). The data fit is performed with the Markov chain Monte Carlo (MCMC) algorithm.

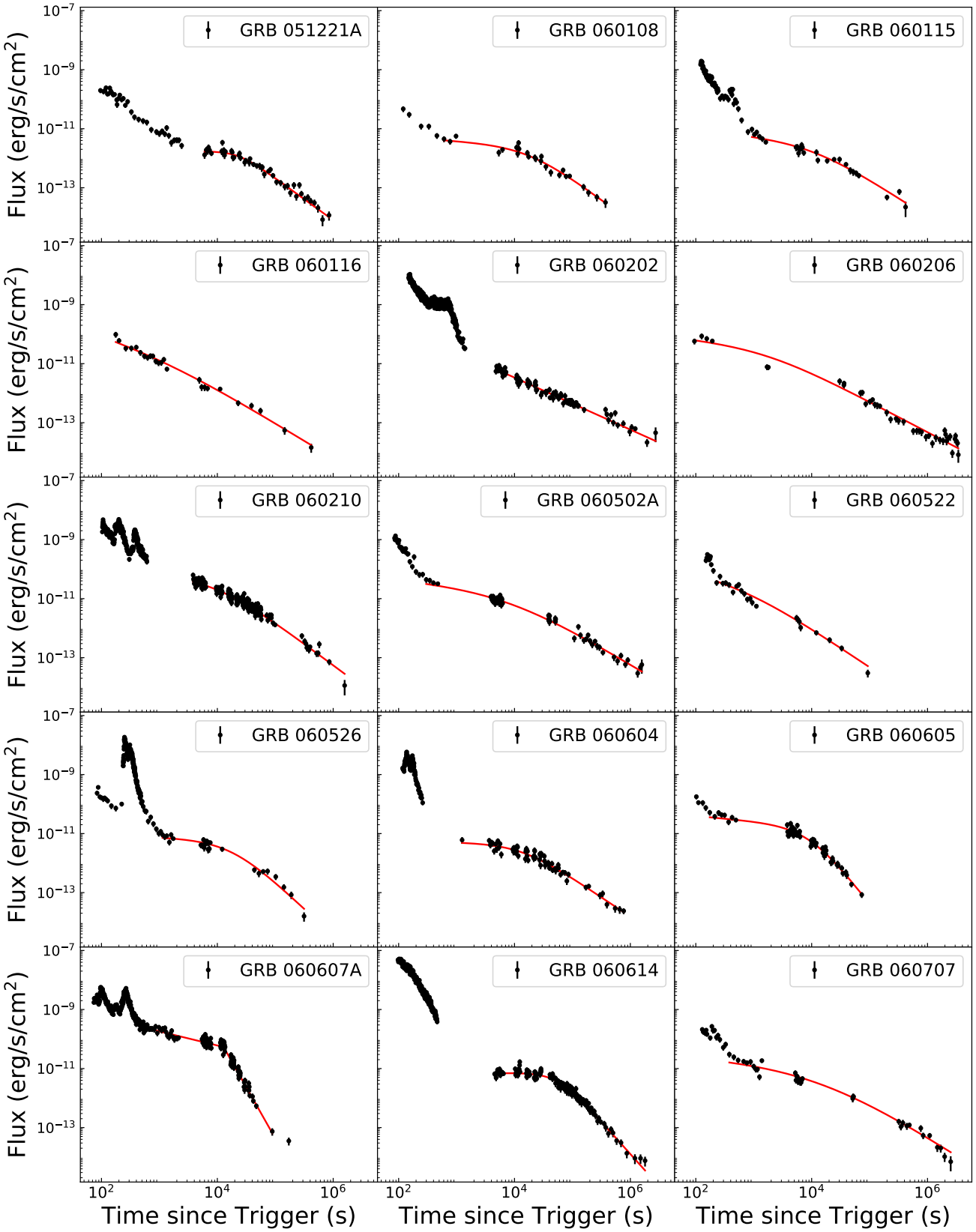

Figure 1. — Continued

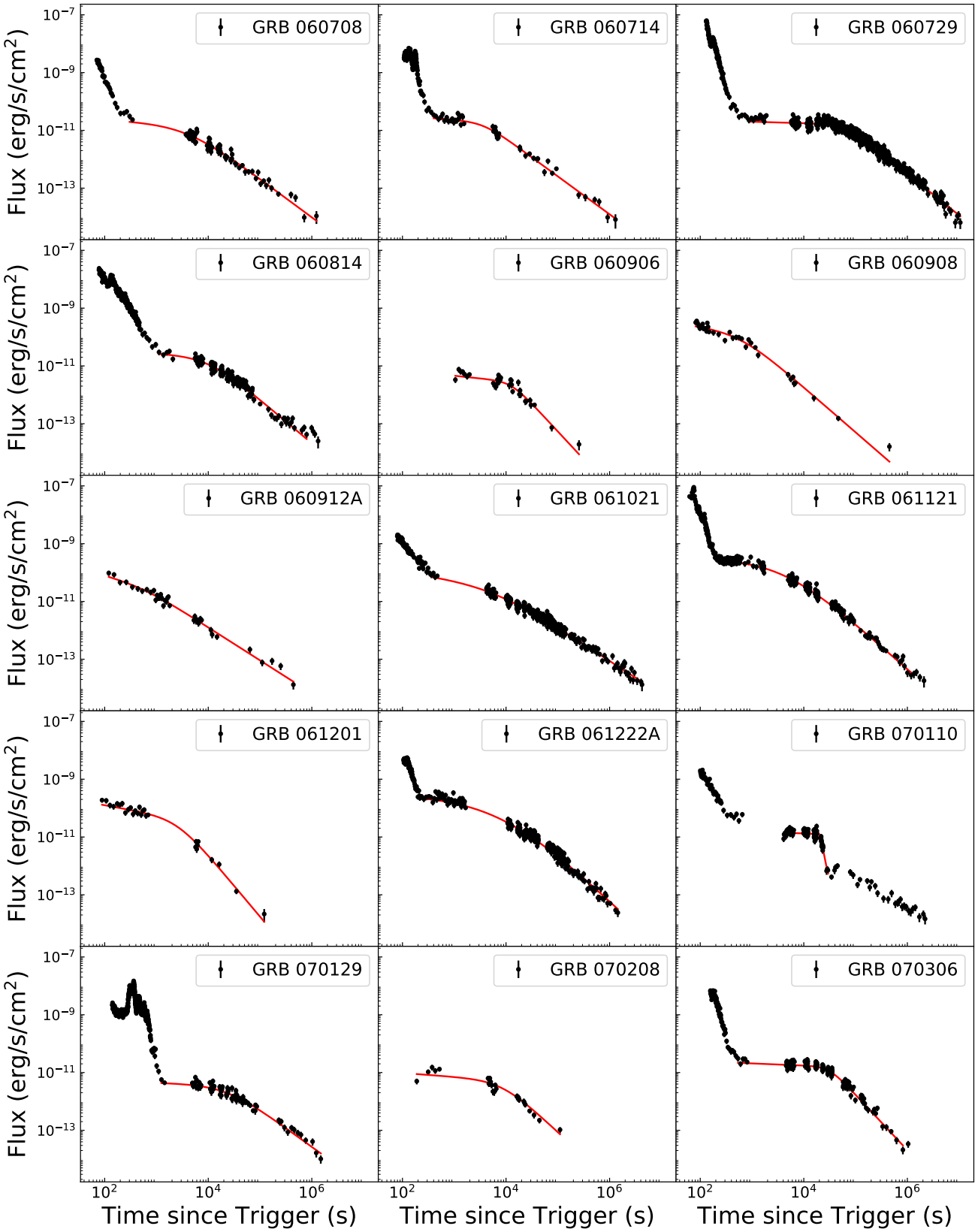

Figure 1. — Continued

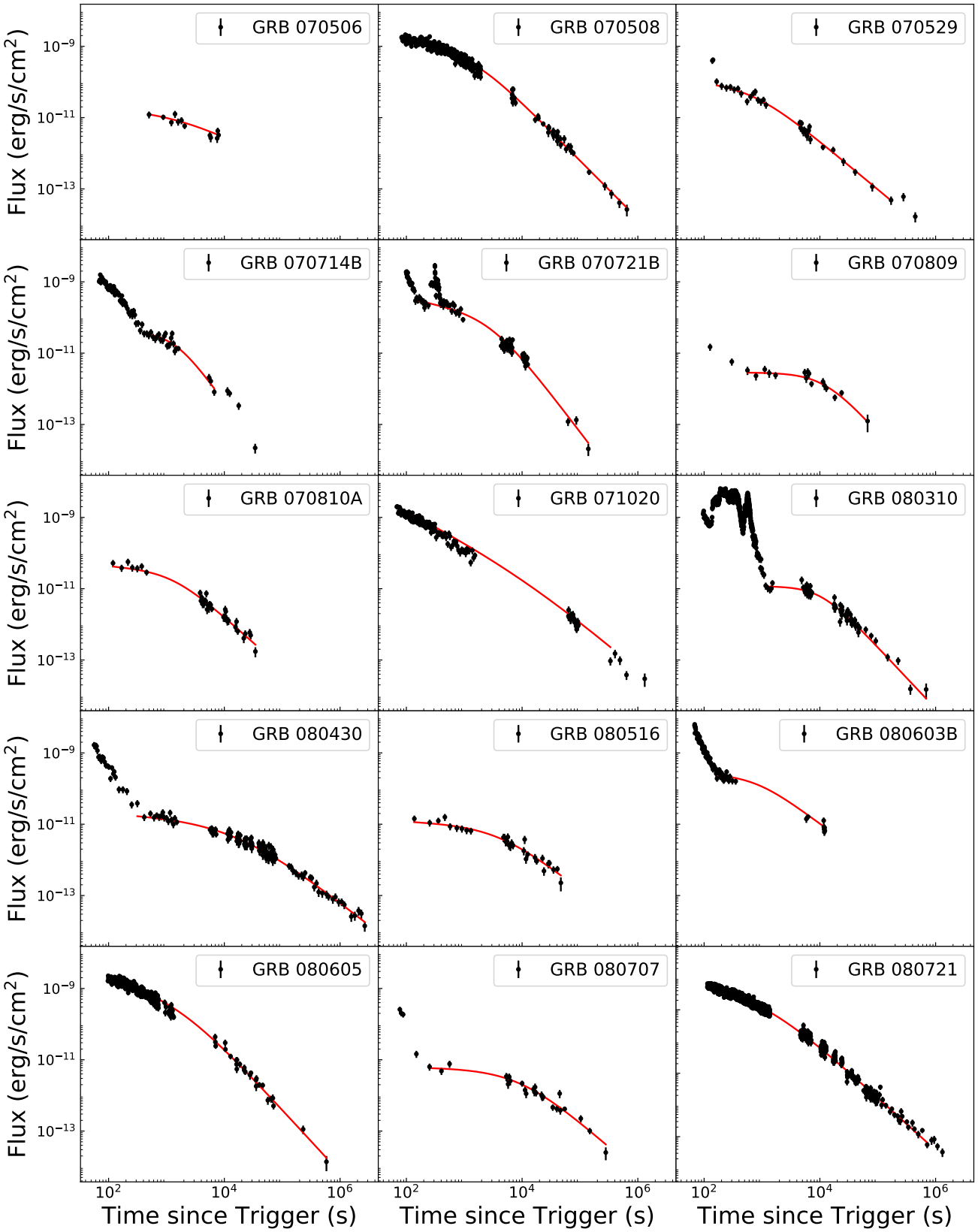

Figure 1. — Continued

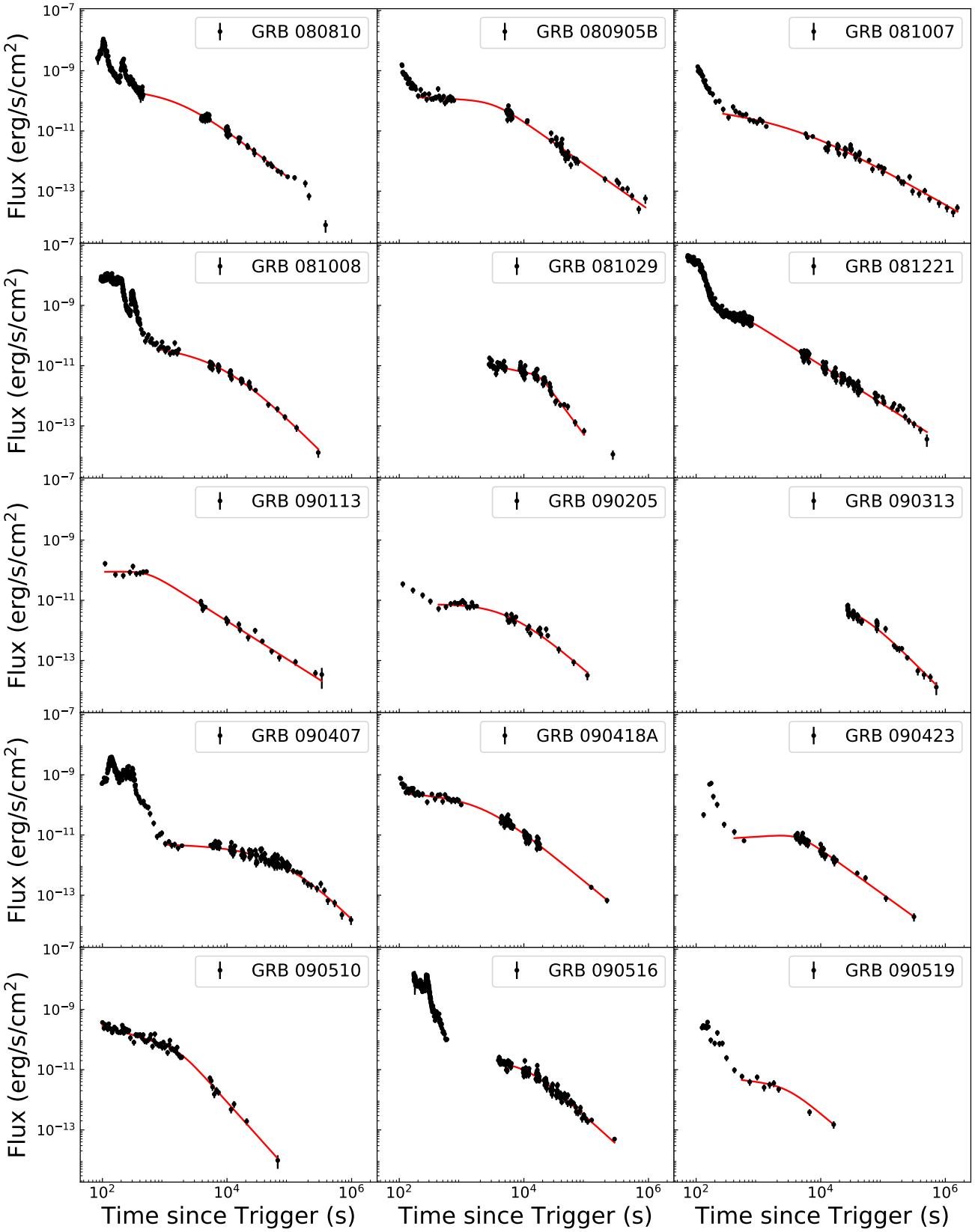

Figure 1. — Continued

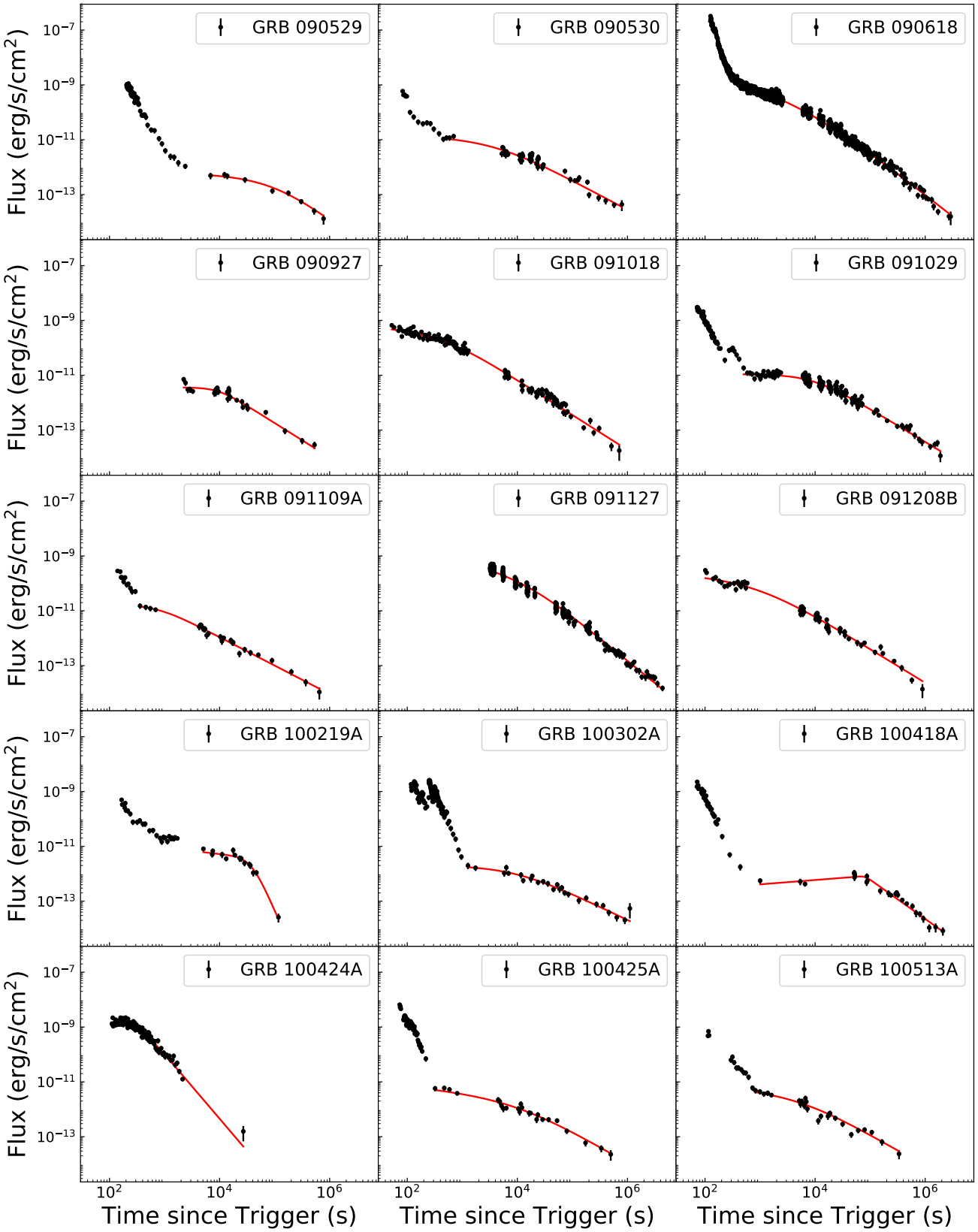

Figure 1. — Continued

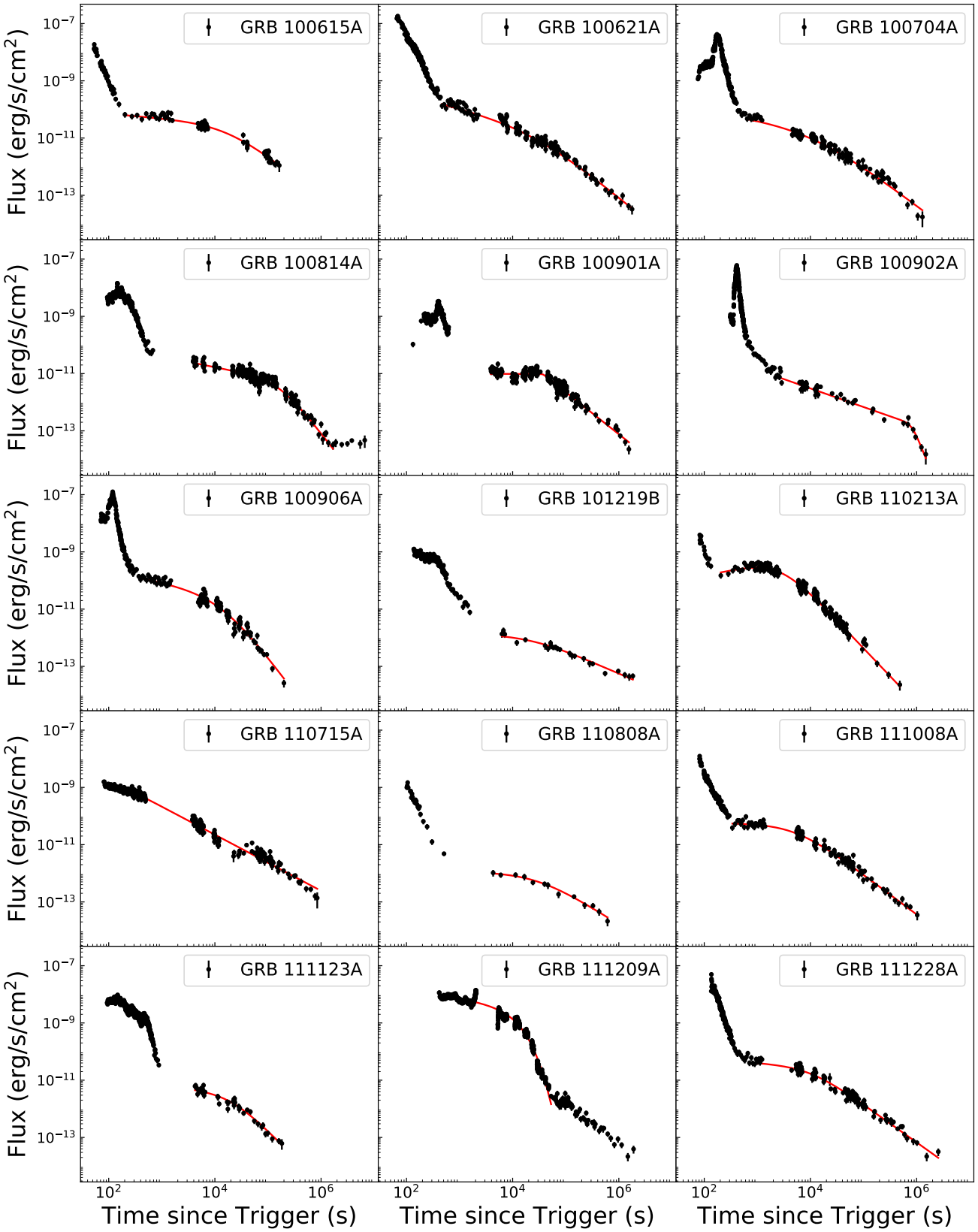

Figure 1. — Continued

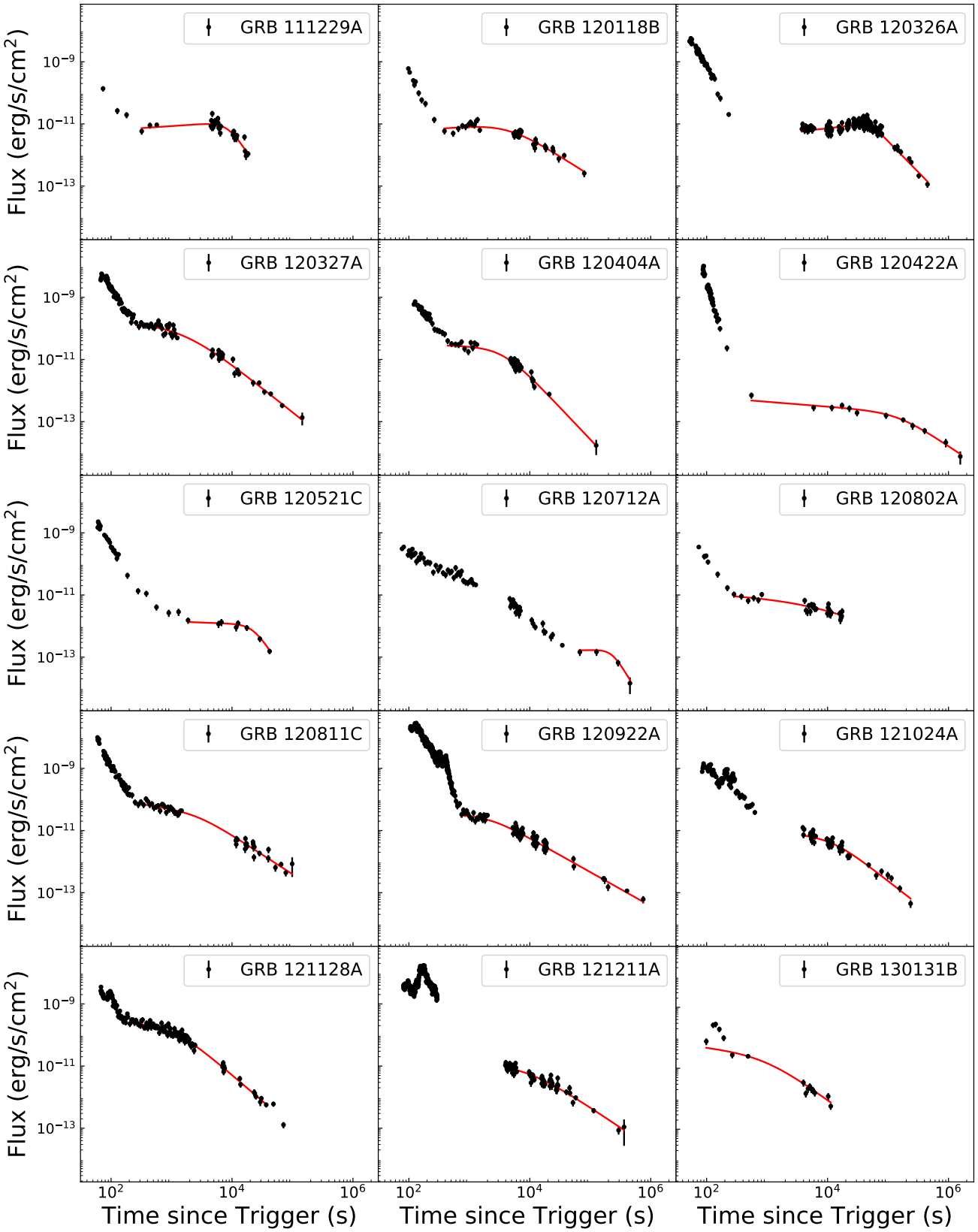

Figure 1. — Continued

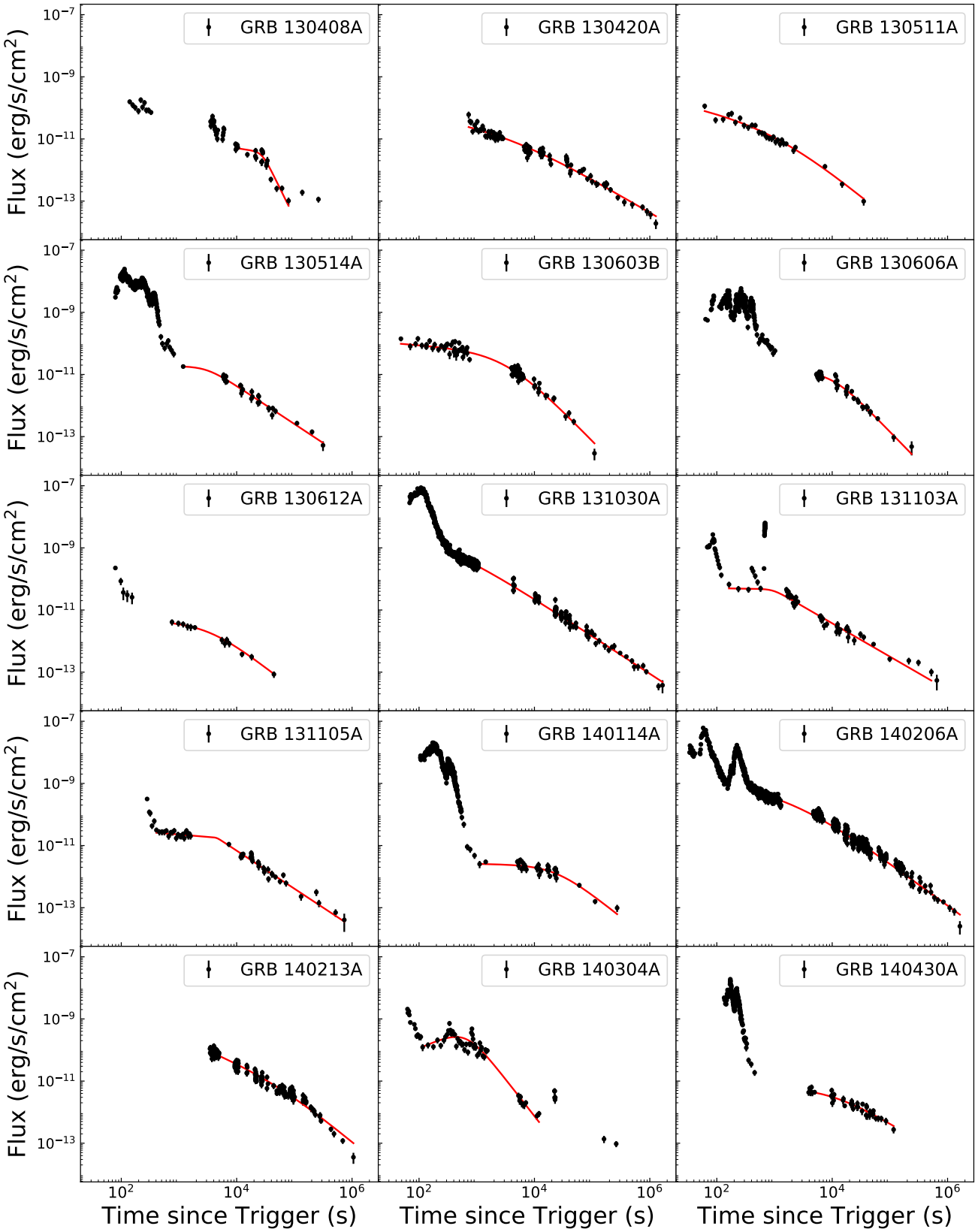

Figure 1. — Continued

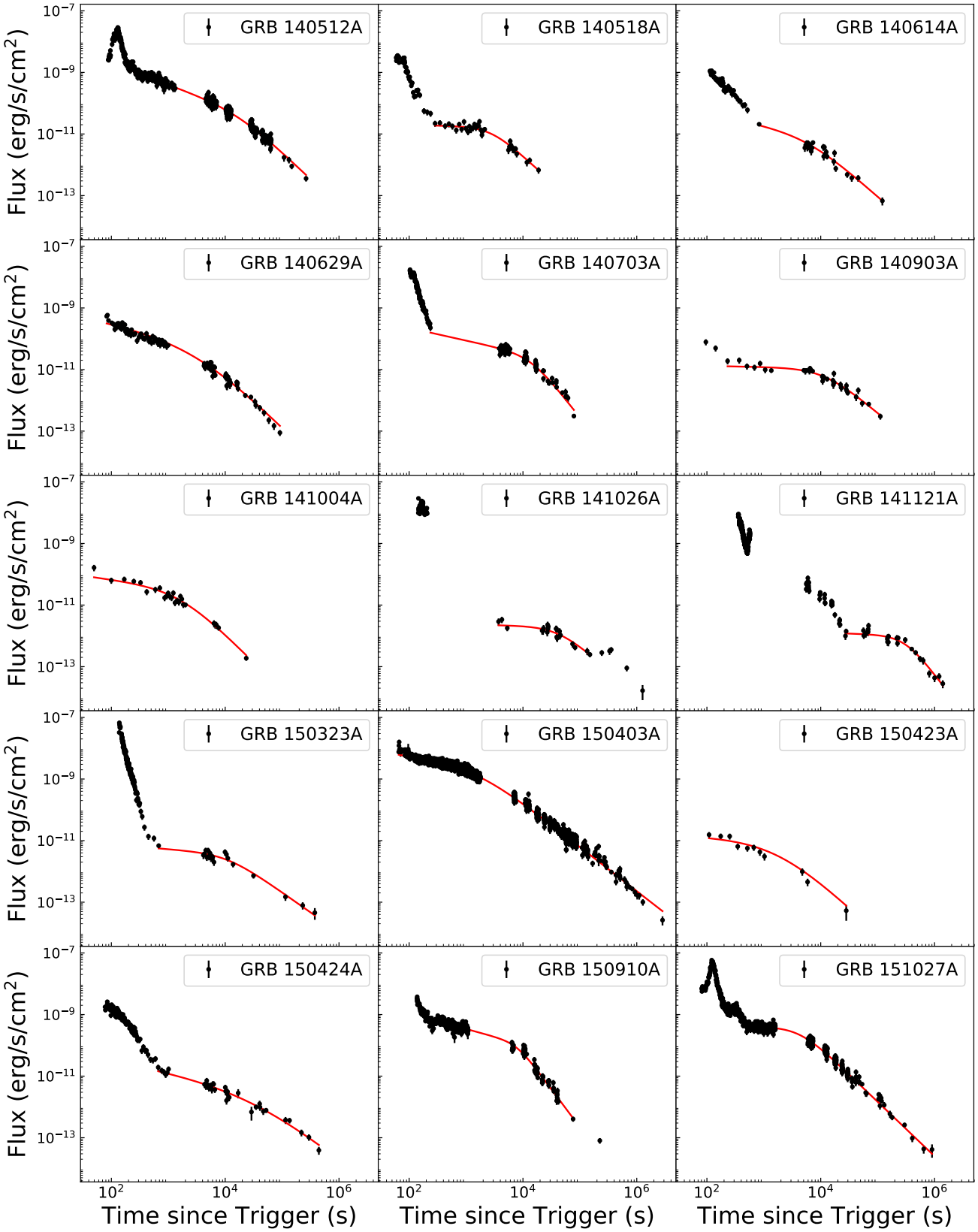

Figure 1. — Continued

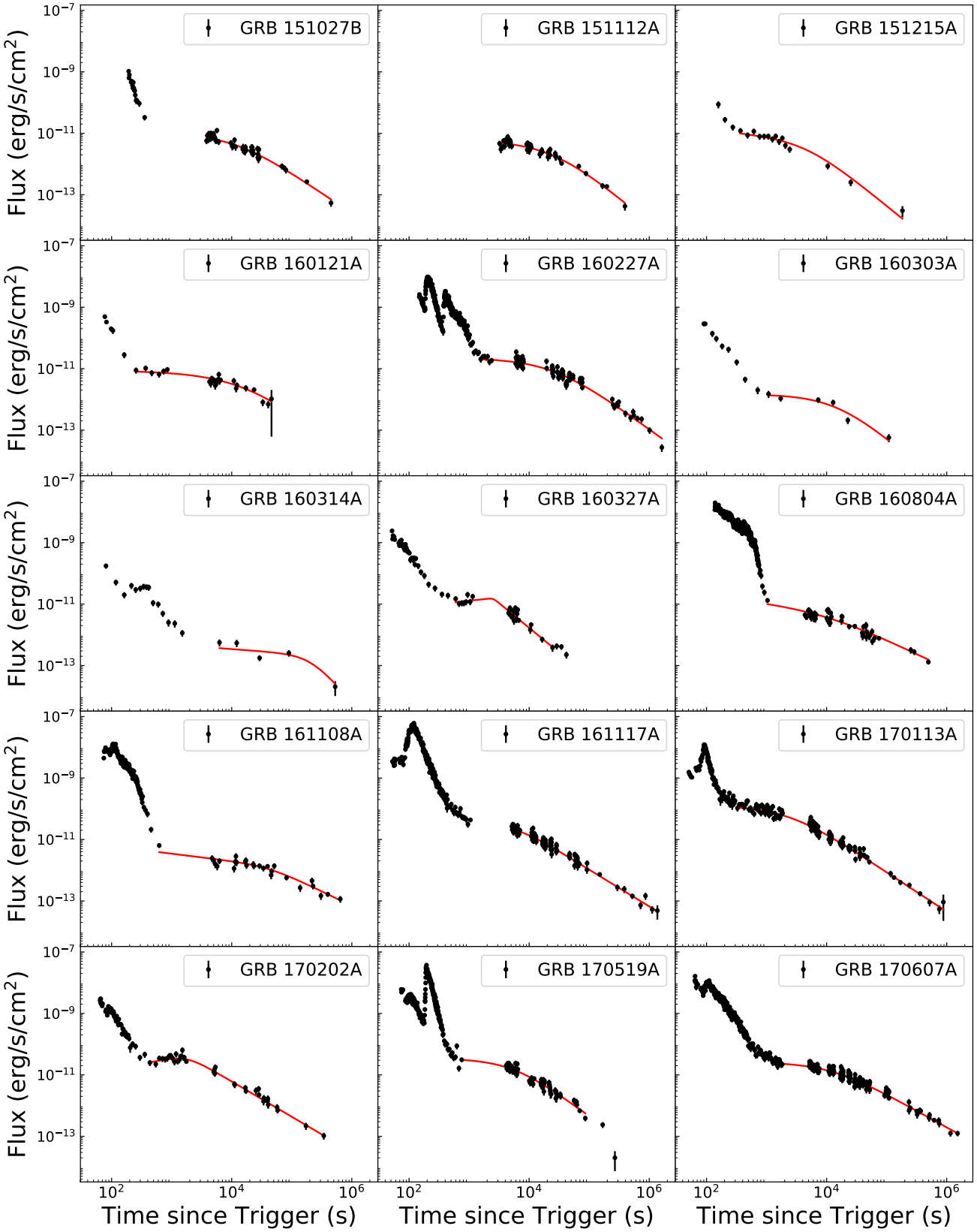

Figure 1. — Continued

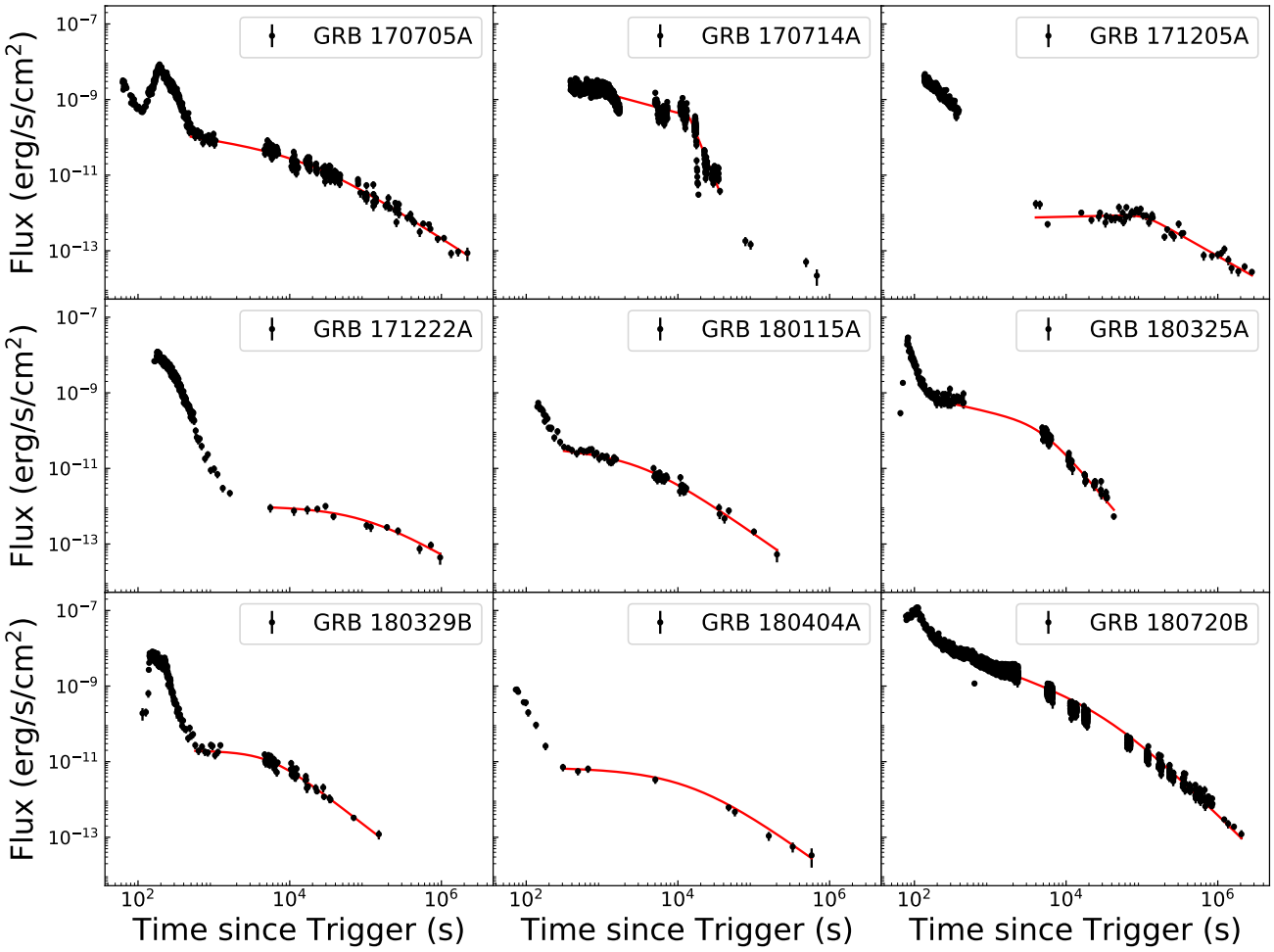

Figure 1. — Continued

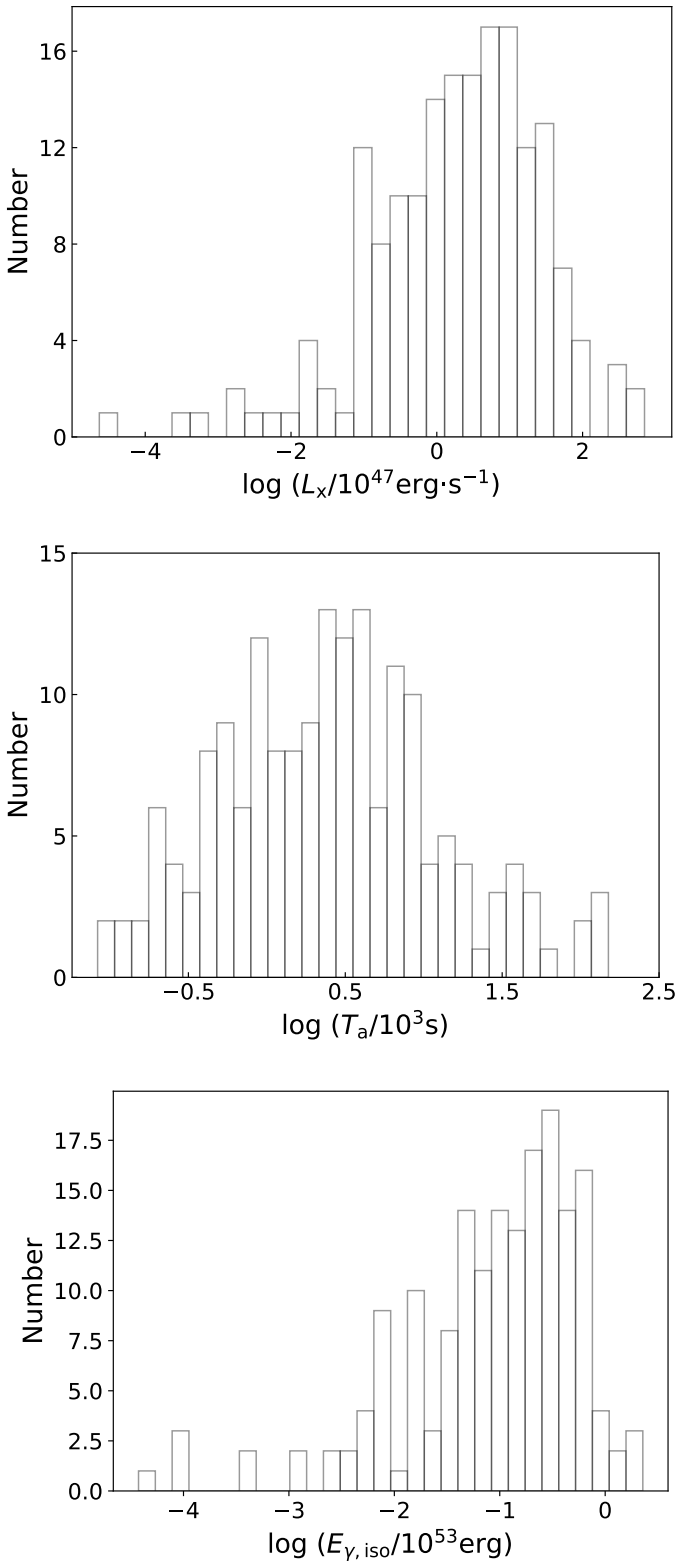

Figure 2. Histograms of L_X, T_a, and $E_{\gamma,\rm iso}$ of our sample. The typical value of $L_{\rm x}$ is 2.6×10^{47} erg·s^{-1} with a 50% distribution range of (0.4, 12)$\times10^{47}$ erg·s^{-1}. The typical value of T_a is 2.4×10^3 s with a 50% distribution range of (0.8, 7)$\times10^3$ s. The typical value of $E_{\gamma,\rm iso}$ is 0.13×10^{53} s, with a 50% distribution range of (0.04, 0.3)$\times10^{53}$ erg.

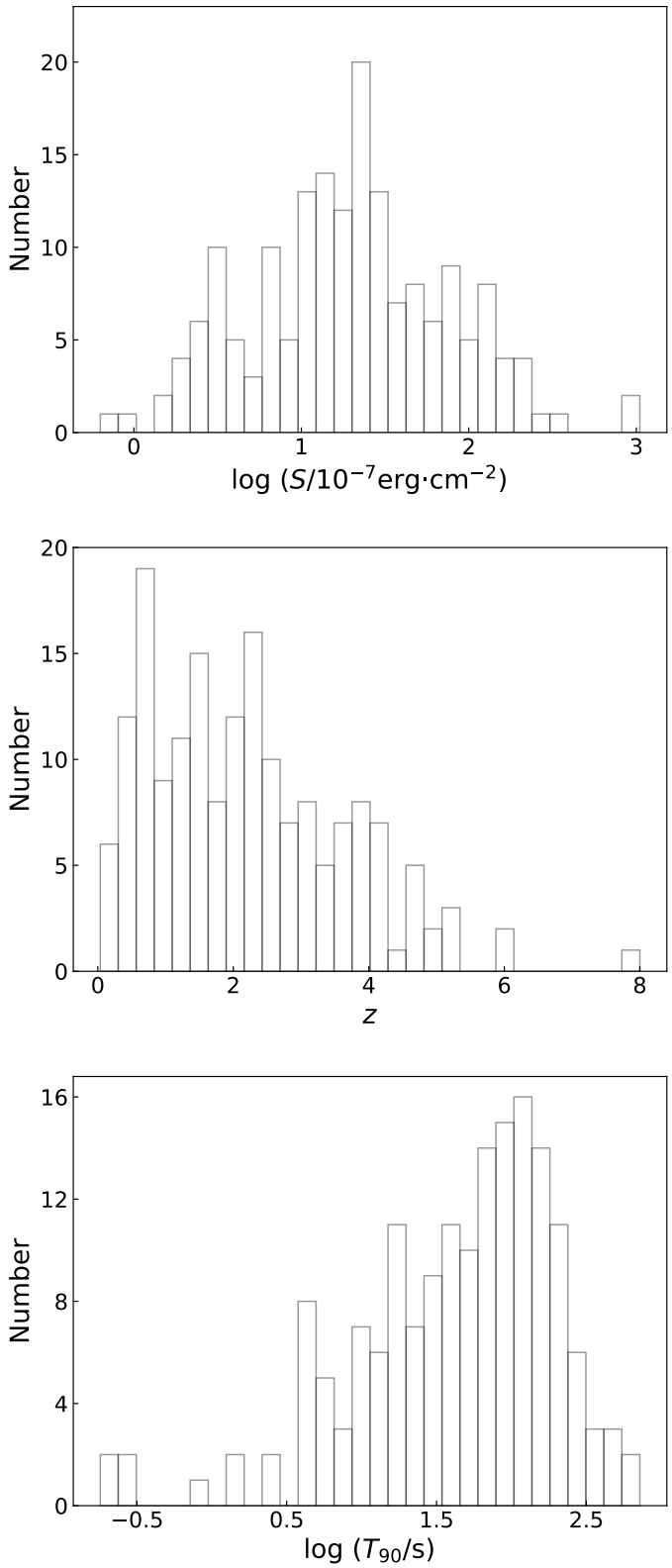

Figure 3. Histograms of S, z, and T_{90} of our sample. The typical value of S is 20×10^{-7} erg·cm^{-2}, with a 50% distribution range of (8, 50)$\times 10^{-7}$ erg·cm^{-2}. The typical value of z is 2.0, with a 50% distribution range of (1.0, 3.2). The typical value of T_{90} is 58 s, with a 50% distribution range of (18, 123) s.

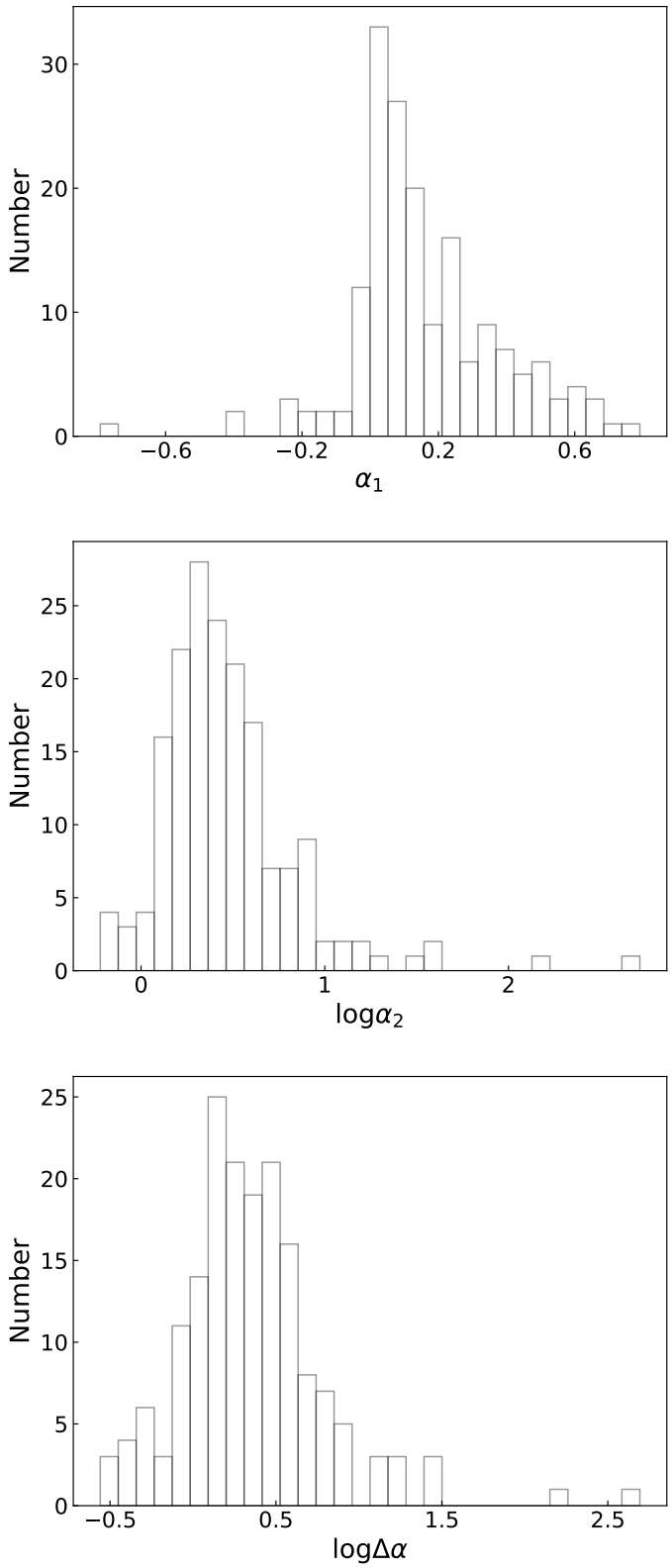

Figure 4. Histograms of α_1, α_2, and $\Delta\alpha$ of our sample. The typical value of α_1 is 0.11, with a 50% distribution range of (0.03, 0.3). The typical value of α_2 is 1.5, with a 50% distribution range of (1.3, 1.9). The typical value of $\Delta\alpha$ is 1.4, with a 50% distribution range of (1.1, 1.7).

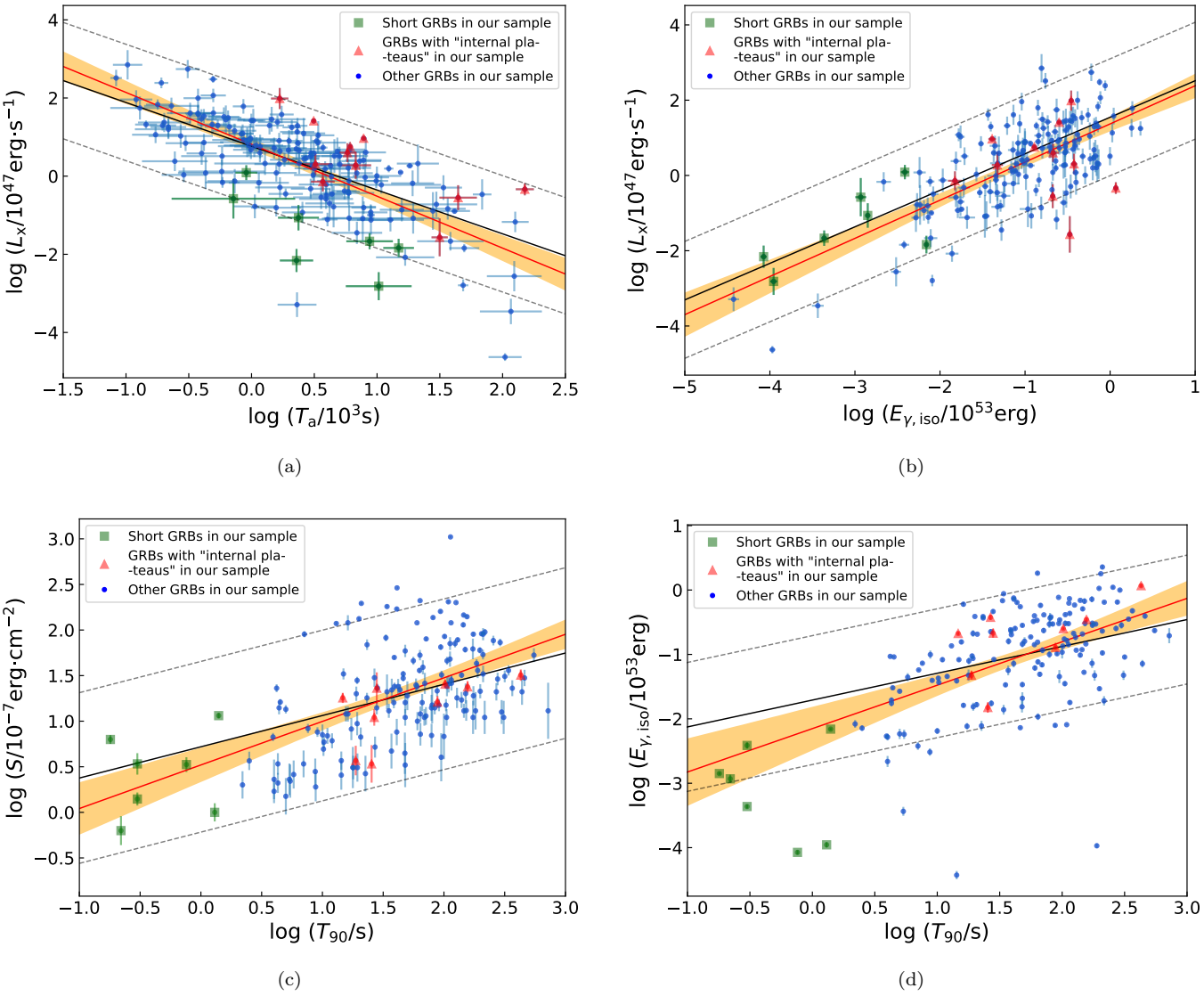

Figure 5. Logarithmic plots of various two-parameter correlations: (a) L_X - T_a, (b) L_X - $E_{\gamma,\mathrm{iso}}$, (c) S - T_{90}, and (d) $E_{\gamma,\mathrm{iso}}$ - T_{90}. 7 short GRBs are marked with green squares, while 11 GRBs with "internal plateaus" are marked with red triangles. The black solid lines are the best fit for the observational data points by the least square linear regression. The black dashed lines are 3σ confidence range. The red solid lines are the best fits by using the bivariate Bayesian linear regression, and the orange regions show the 3σ ranges correspondingly.

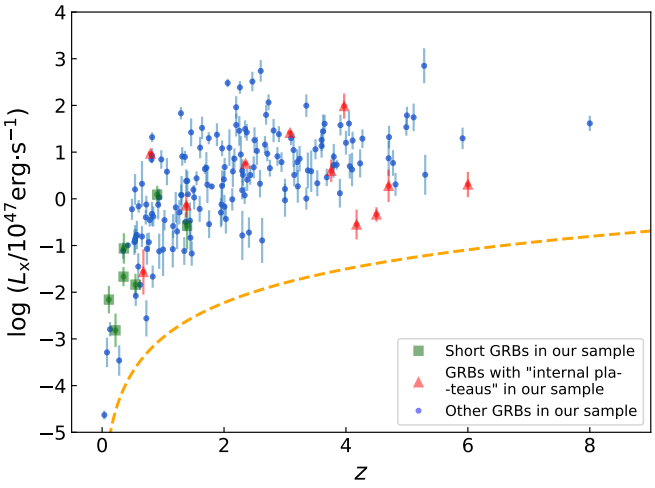

(a)

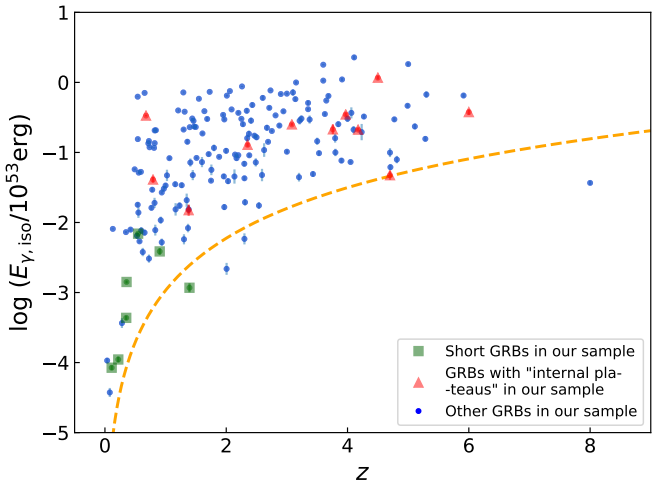

(b)

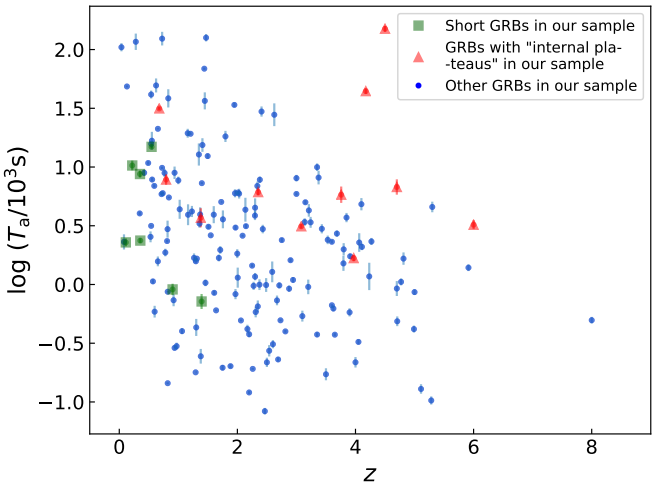

(c)

Figure 6. Dependence of L_X, $E_{\gamma,\rm iso}$, and T_a on redshifts. Panel (a) shows L_X versus z. The dashed line represents the XRT detection limit of $f_{\rm lim} \sim 2\times10^{-14}$ erg cm^{-2} s^{-1}. Panel (b) shows $E_{\gamma,\rm iso}$ versus z. The dashed line represents the BAT detection limit of $f_{\rm lim} \sim 10^{-8}$ erg cm^{-2} s^{-1} by assuming a GRB duration of 2 s. Panel (c) illustrates T_a versus z.

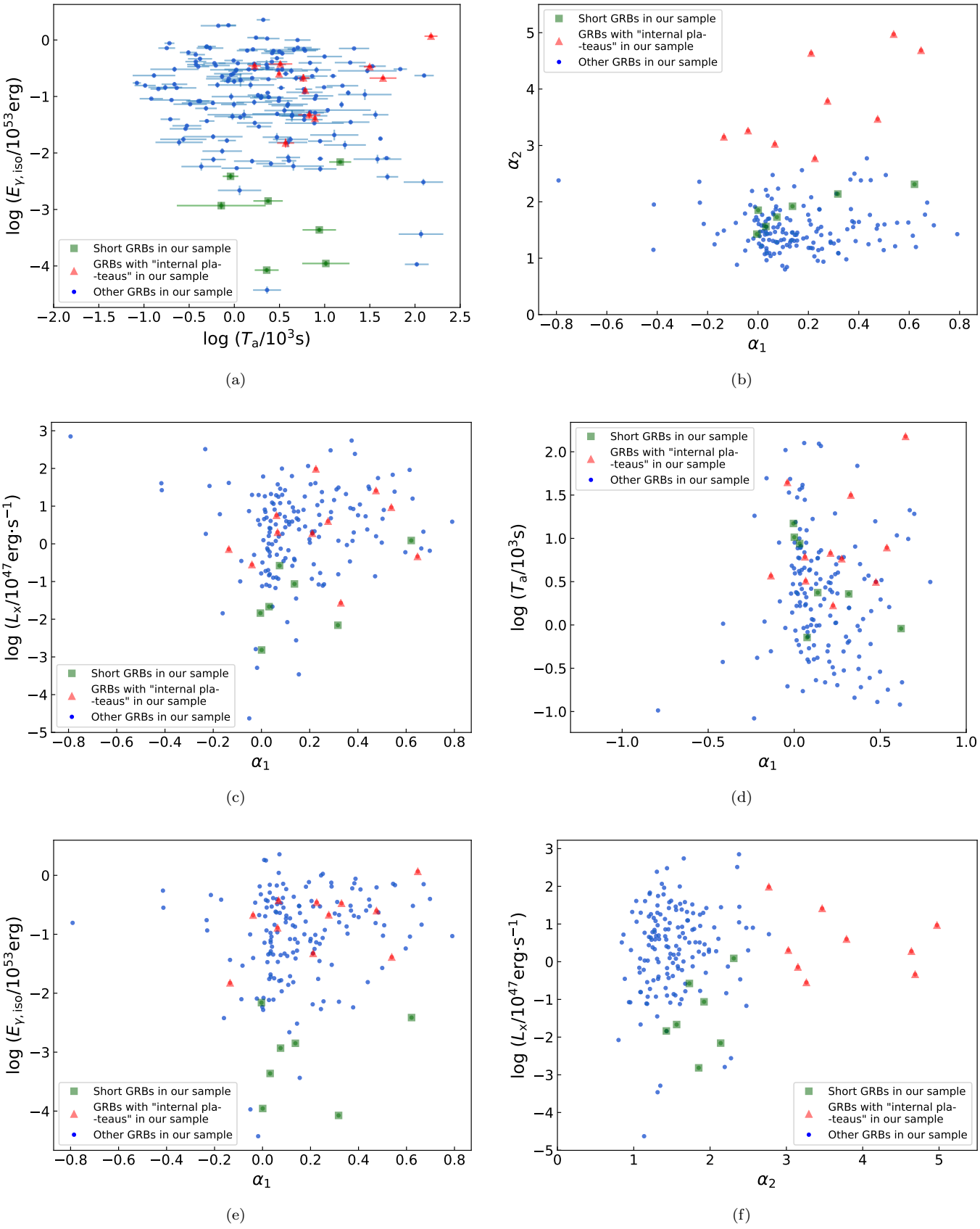

Figure 7. Logarithmic plots between various parameter pairs. Here, T_a is the end time of the plateau, L_X is the luminosity at the end time, $E_{\gamma,\mathrm{iso}}$ is the isotropic energy of the prompt emission, α_1 is the power-law timing index during the plateau phase and α_2 is the power-law timing index in the following decay phase, and finally T_{90} is the GRB duration. In order to clearly demonstrate the distributions, we do not show the error bars in 7 of the plots (Panels 7b, 7c, 7d, 7e, 7f, 7a, and 7h).

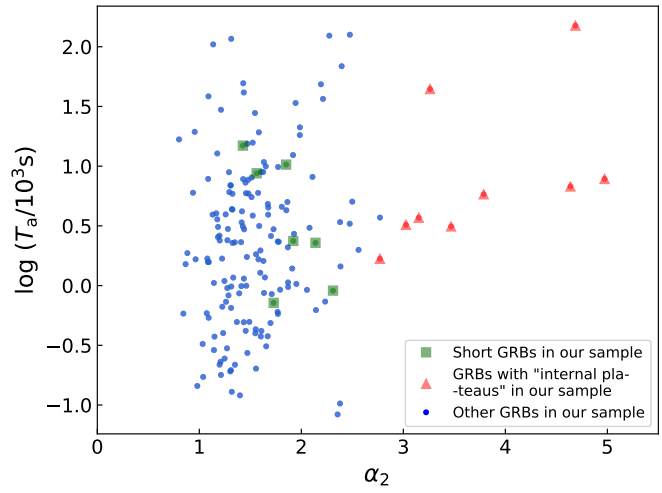

(g)

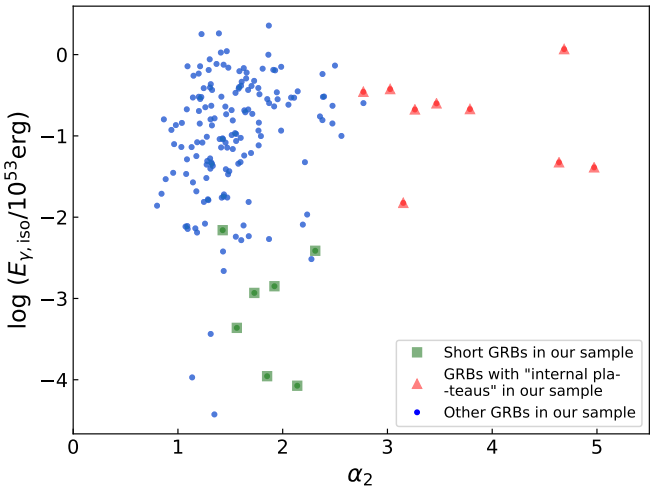

(h)

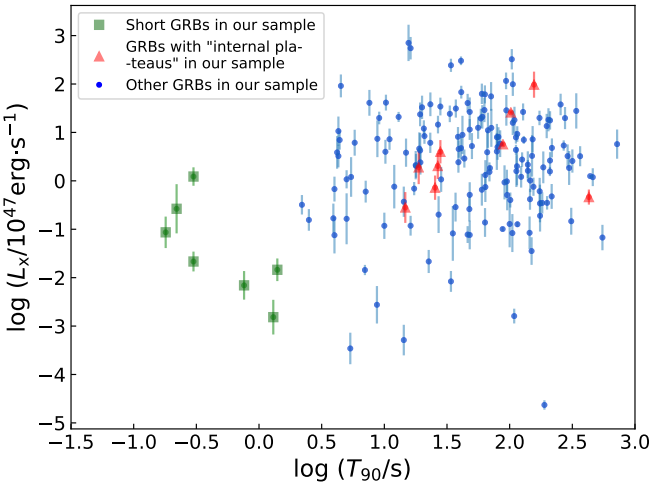

(i)

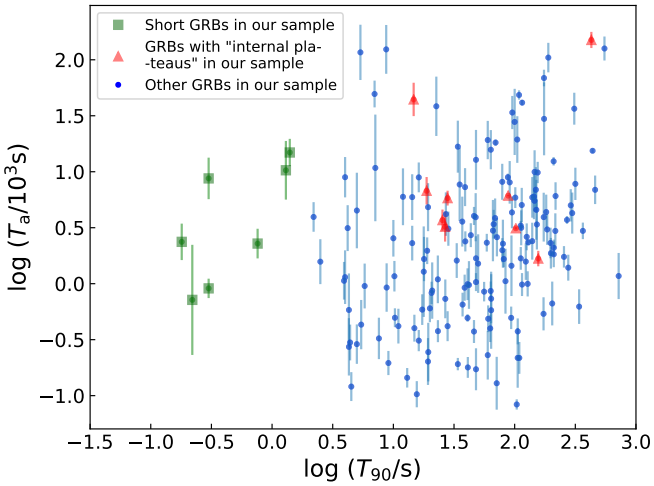

(j)

Figure 7. — Continued

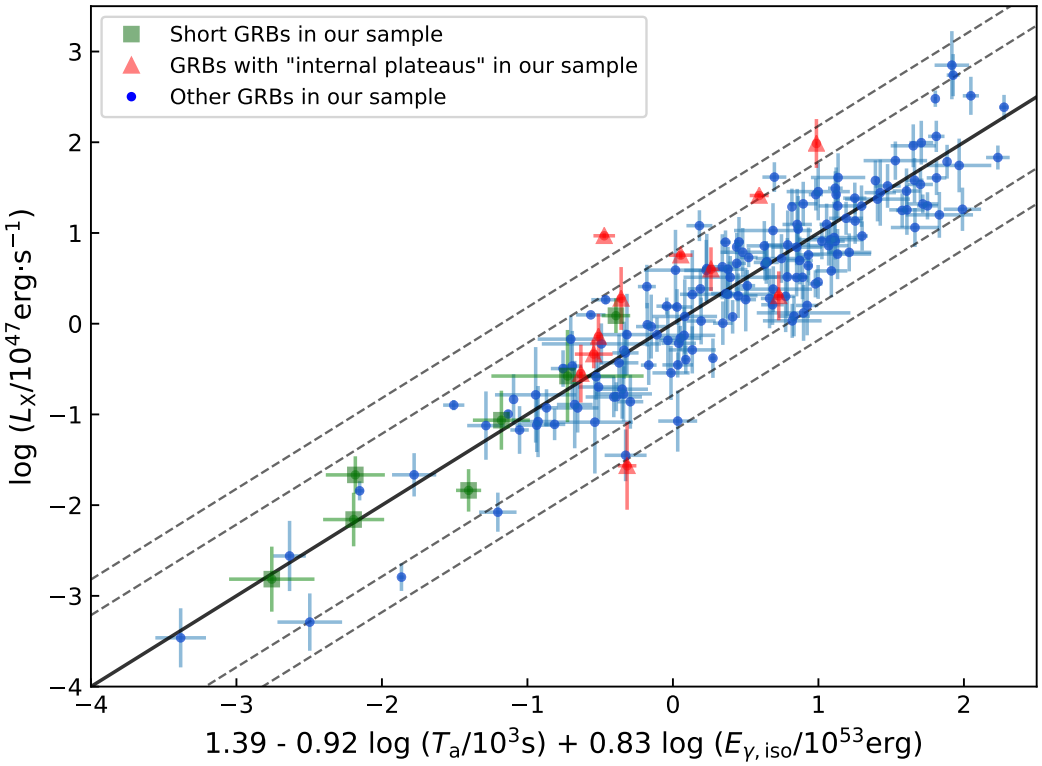

Figure 8. The best-fit L-T-E correlation by using all the 174 GRBs of our sample. Here, L_X is the luminosity at the end time of the plateau, T_a is the corresponding end time, and $E_{\gamma,\rm iso}$ is the isotropic γ-ray energy of the prompt emission. The black solid lines are the best fit for the observational data points. The black dashed lines are error lines of 2σ and 3σ confidence intervals.

Table 3. Fitting Results and Some Key Parameters of the 174 GRBs in Our Sample

GRB Name	T_{90}^a	z^a	S(15-150 keV)^a	α_1^b	α_2^b	$\log(T_a/10^3)^b$	$\log(L_X/10^{47})^c$	$\log(E'_{\gamma,\rm iso}/10^{53})^d$	$\log(E_{\gamma,\rm iso}/10^{53})^e$
	(s)		(10^{-7} erg/cm^2)			(s)	(erg/s)	(erg)	(erg)
GRB 050315	95.6	1.949	32.2±1.46	-0.03±0.05	1.94±0.25	1.53±0.15	-0.29±0.32	-0.52±0.02	-0.46±0.02
GRB 050319	152.5	3.24	13.1±1.48	0.15±0.11	1.41±0.17	0.53±0.22	0.86±0.27	-0.53±0.05	-0.52±0.05
GRB 050401	33.3	2.9	82.2±3.06	0.55±0.03	1.63±0.28	0.21±0.16	1.38±0.17	0.19±0.02	-0.17±0.02
GRB 050416A	2.5	0.6535	3.67±0.37	0.32±0.09	1.09±0.09	0.2±0.2	-0.81±0.22	-2.38±0.04	-2.14±0.04
GRB 050505	58.9	4.27	24.9±1.79	0.06±0.14	1.78±0.11	0.37±0.08	1.29±0.2	-0.06±0.03	-0.49±0.03
GRB 050730	156.5	3.97	23.8±1.52	0.23±0.1	2.77±0.19	0.22±0.07	1.99±0.27	-0.13±0.03	-0.46±0.03
GRB 050801	19.4	1.38	3.1±0.48	0.44±0.45	1.25±0.15	-0.61±0.26	0.38±0.25	-1.81±0.06	-1.81±0.06
GRB 050802	19	1.71	20±1.57	0.5±0.19	1.6±0.08	0.29±0.12	0.67±0.34	-0.82±0.03	-1.02±0.03
GRB 050803	87.9	0.422	21.5±1.35	-0.09±0.11	1.63±0.05	0.95±0.03	-1±0.04	-2.01±0.03	-2.1±0.03
GRB 050814	150.9	5.3	20.1±2.2	0.06±0.14	1.81±0.34	0.66±0.27	0.52±0.43	-0.01±0.05	-0.17±0.05
GRB 050824	22.6	0.83	2.66±0.52	0.05±0.13	1.09±0.23	1.58±0.27	-1.67±0.24	-2.31±0.08	-2.11±0.08
GRB 050922C	4.5	2.199	16.2±0.54	0.61±0.09	1.4±0.07	-0.92±0.13	1.96±0.24	-0.72±0.01	-1.04±0.01
GRB 051016B	4	0.9364	1.7±0.22	0±0.09	1.6±0.18	0.95±0.18	-1.12±0.38	-2.4±0.05	-2.28±0.05
GRB 051109A	37.2	2.346	22±2.72	0.32±0.08	1.31±0.05	-0.19±0.11	1.49±0.19	-0.54±0.05	-0.8±0.05
GRB 051109B	14.3	0.08	2.56±0.41	-0.02±0.15	1.35±0.16	0.36±0.15	-3.29±0.32	-4.43±0.06	-4.43±0.06
GRB 051221A	1.4	0.547	11.5±0.35	0±0.22	1.43±0.11	1.17±0.12	-1.84±0.23	-2.04±0.01	-2.16±0.01
GRB 060108	14.3	2.03	3.69±0.37	0.14±0.13	1.46±0.22	0.77±0.2	-0.43±0.31	-1.42±0.04	-1.41±0.04
GRB 060115	139.6	3.53	17.1±1.5	0.22±0.18	1.28±0.17	0.38±0.16	0.33±0.28	-0.35±0.04	-1.01±0.04
GRB 060116	105.9	4	24.1±2.61	0.63±0.24	1.2±0.17	-0.66±0.27	1.2±0.25	-0.12±0.04	-0.52±0.04
GRB 060202	198.9	0.78	21.3±1.65	-0.08±0.29	0.88±0.03	0.27±0.14	-0.45±0.14	-1.46±0.03	-1.53±0.03
GRB 060206	7.6	4.05	8.31±0.42	0.22±0.17	1.03±0.07	-0.49±0.19	1.61±0.27	-0.57±0.02	-1.14±0.02
GRB 060210	255	3.91	76.6±4.09	0.07±0.16	1.47±0.08	0.24±0.1	1.58±0.22	0.37±0.02	0.04±0.02
GRB 060502A	28.4	1.51	23.1±1.02	0.2±0.11	1.18±0.08	0.49±0.15	0.03±0.26	-0.86±0.02	-1.08±0.02
GRB 060522	71.1	5.11	11.4±1.11	0.48±0.35	1.32±0.17	-0.89±0.24	1.74±0.3	-0.28±0.04	-0.63±0.04
GRB 060526	298.2	3.21	12.6±1.65	0.09±0.17	1.85±0.28	0.63±0.18	0.27±0.35	-0.55±0.05	-0.55±0.05
GRB 060604	95	2.1357	4.02±1.06	0.04±0.17	1.32±0.11	0.64±0.14	-0.01±0.24	-1.35±0.1	-1.34±0.1
GRB 060605	79.1	3.8	6.97±0.9	0.17±0.12	2.56±0.27	0.3±0.11	0.9±0.27	-0.69±0.05	-1±0.05
GRB 060607A	102.2	3.082	25.5±1.12	0.47±0.02	3.47±0.1	0.5±0.01	1.41±0.02	-0.28±0.02	-0.6±0.02
GRB 060614	108.7	0.13	204±3.63	-0.02±0.05	2.19±0.13	1.69±0.04	-2.79±0.15	-2.09±0.01	-2.09±0.01
GRB 060707	66.2	3.43	16±1.51	0.13±0.14	1.28±0.16	0.47±0.27	0.59±0.44	-0.4±0.04	-1.31±0.04
GRB 060708	10.2	2.3	4.94±0.37	0.1±0.16	1.33±0.1	0.07±0.14	0.6±0.25	-1.2±0.03	-1.37±0.03
GRB 060714	115	2.71	28.3±1.67	0.13±0.15	1.31±0.06	-0.01±0.1	0.97±0.16	-0.32±0.02	-0.36±0.02
GRB 060729	115.3	0.54	26.1±2.11	0.05±0.04	1.44±0.02	1.62±0.02	-0.9±0.06	-1.7±0.03	-1.75±0.03
GRB 060814	145.3	0.84	146±2.39	0.1±0.17	1.51±0.08	0.74±0.1	-0.38±0.22	-0.56±0.01	-0.68±0.01
GRB 060906	43.5	3.685	22.1±1.36	0.18±0.14	1.93±0.4	0.43±0.11	0.46±0.19	-0.21±0.03	-0.19±0.03
GRB 060908	19.3	1.8836	28±1.11	0.25±0.19	1.56±0.18	-0.7±0.21	1.37±0.25	-0.6±0.02	-1.06±0.02
GRB 060912A	5	0.937	13.5±0.62	0.5±0.2	1.14±0.06	-0.54±0.18	0.03±0.19	-1.5±0.02	-1.57±0.02

Table 3 continued on next page

Table 3 *(continued)*

GRB Name	T_{90}^a (s)	z^a	S(15-150 keV)^a (10^{-7} erg/cm^2)	α_1^b	α_2^b	$\log(T_a/10^3)^b$ (s)	$\log(L_X/10^{47})^c$ (erg/s)	$\log(E'_{\gamma,\rm iso}/10^{53})^d$ (erg)	$\log(E_{\gamma,\rm iso}/10^{53})^e$ (erg)
GRB 061021	46.2	0.3463	29.6±1.01	0.25±0.09	1.17±0.04	0.6±0.08	-1.11±0.17	-2.05±0.01	-2.14±0.01
GRB 061121	81.3	1.314	137±1.99	0.01±0.05	1.58±0.06	0.22±0.07	0.91±0.2	-0.2±0.01	-0.42±0.01
GRB 061201	0.76	0.111	3.34±0.27	0.32±0.16	2.14±0.28	0.36±0.13	-2.16±0.3	-4.02±0.03	-4.07±0.03
GRB 061222A	71.4	2.088	79.9±1.58	0.04±0.07	1.7±0.14	0.42±0.17	1.09±0.39	-0.07±0.01	-0.39±0.01
GRB 070110	88.4	2.352	16.2±1.08	0.06±0.06	8.95±0.62	0.79±0.01	0.76±0.04	-0.67±0.03	-0.89±0.03
GRB 070129	460.6	2.3384	29.8±2.67	0.06±0.11	1.31±0.11	0.84±0.13	0.08±0.18	-0.41±0.04	-0.4±0.04
GRB 070208	47.7	1.165	4.45±1.01	0.13±0.14	1.67±0.42	0.59±0.21	-0.58±0.25	-1.79±0.09	-1.81±0.09
GRB 070306	209.5	1.497	53.8±2.86	0.07±0.05	1.92±0.1	1.09±0.04	0.19±0.1	-0.5±0.02	-0.64±0.02
GRB 070506	4.3	2.31	2.1±0.23	0.11±0.33	0.84±0.36	-0.23±0.33	0.51±0.23	-1.57±0.05	-1.71±0.05
GRB 070508	20.9	0.82	196±2.73	0.38±0.07	1.63±0.27	-0.06±0.25	0.93±0.16	-0.45±0.01	-0.69±0.01
GRB 070529	109.2	2.4996	25.7±2.45	0.18±0.21	1.35±0.1	-0.66±0.14	1.26±0.28	-0.42±0.04	-0.78±0.04
GRB 070714B	64	0.92	7.2±0.9	0.08±0.33	2.23±0.62	-0.13±0.22	-0.13±0.31	-1.79±0.05	-1.97±0.05
GRB 070721B	340	3.626	36±2	0.31±0.12	2.14±0.25	-0.2±0.15	1.44±0.36	-0.01±0.02	-0.45±0.02
GRB 070809	1.3	0.22	1±0.1	0±0.15	1.85±0.85	1.01±0.26	-2.82±0.36	-3.93±0.04	-3.96±0.04
GRB 070810A	11	2.17	6.9±0.6	0.13±0.16	1.45±0.15	-0.38±0.16	0.86±0.22	-1.1±0.04	-1.08±0.04
GRB 071020	4.2	2.145	23±1	0.79±0.07	1.43±0.41	0.5±0.2	0.59±0.34	-0.59±0.02	-1.03±0.02
GRB 080310	365	2.43	23±2	-0.01±0.08	1.73±0.13	0.47±0.07	0.51±0.21	-0.49±0.04	-0.32±0.04
GRB 080430	16.2	0.767	12±1	0.07±0.07	1.29±0.08	0.95±0.13	-0.93±0.2	-1.72±0.03	-1.79±0.03
GRB 080516	5.8	3.2	2.6±0.4	0.08±0.13	1.27±0.24	-0.02±0.2	0.79±0.27	-1.24±0.06	-1.35±0.06
GRB 080603B	60	2.69	24±1	0.13±0.23	1.21±0.27	-0.64±0.22	1.8±0.21	-0.4±0.02	-0.85±0.02
GRB 080605	20	1.6398	133±2	0.44±0.08	1.77±0.26	-0.22±0.12	1.52±0.24	-0.04±0.01	-0.41±0.01
GRB 080707	27.1	1.23	5.2±0.6	0.03±0.13	1.42±0.21	0.62±0.19	-0.7±0.38	-1.68±0.05	-1.76±0.05
GRB 080721	16.2	2.602	120±10	0.37±0.05	1.66±0.05	-0.51±0.09	2.74±0.23	0.27±0.03	-0.22±0.03
GRB 080810	106	3.35	46±2	0.08±0.15	1.6±0.11	-0.43±0.12	2±0.24	0.04±0.02	-0.38±0.02
GRB 080905B	128	2.374	18±2	0.1±0.15	1.46±0.07	0±0.11	1.42±0.18	-0.62±0.05	-0.73±0.05
GRB 081007	10	0.5295	7.1±0.8	0.21±0.11	1.18±0.08	0.41±0.16	-0.93±0.27	-2.28±0.05	-2.19±0.05
GRB 081008	185.5	1.9685	43±2	0.21±0.14	2.08±0.21	0.48±0.14	0.28±0.33	-0.38±0.02	-0.53±0.02
GRB 081029	270	3.8479	21±2	0.43±0.07	2.77±0.3	0.57±0.04	0.73±0.11	-0.21±0.04	-0.6±0.04
GRB 081221	34	2.26	181±3	0.39±0.11	1.3±0.02	-0.72±0.06	2.39±0.14	0.35±0.01	-0.06±0.01
GRB 090113	9.1	1.7493	7.6±0.4	-0.04±0.16	1.31±0.06	-0.71±0.11	1.3±0.13	-1.23±0.02	-1.4±0.02
GRB 090205	8.8	4.7	1.9±0.3	-0.05±0.15	1.79±0.32	-0.03±0.22	0.87±0.38	-1.12±0.06	-1±0.06
GRB 090313	79	3.375	14±2	0.04±0.42	2.11±0.27	0.91±0.16	0.61±0.38	-0.47±0.06	-0.53±0.06
GRB 090407	310	1.4485	11±2	0.03±0.08	2.21±0.27	1.56±0.14	-0.83±0.28	-1.22±0.07	-1.32±0.07
GRB 090418A	56	1.608	46±2	0.11±0.12	1.71±0.1	-0.07±0.09	1.1±0.23	-0.51±0.02	-0.73±0.02
GRB 090423	10.3	8	5.9±0.4	-0.14±0.14	1.49±0.11	-0.3±0.08	1.62±0.16	-0.29±0.03	-1.43±0.03
GRB 090510	0.3	0.903	3.4±0.4	0.62±0.07	2.31±0.25	-0.04±0.09	0.09±0.19	-2.13±0.05	-2.41±0.05
GRB 090516	210	4.109	90±6	0.07±0.23	1.87±0.14	0.32±0.07	1.25±0.19	0.47±0.03	0.36±0.03
GRB 090519	64	3.9	12±1	0.2±0.42	1.77±0.84	-0.24±0.34	0.12±0.31	-0.44±0.03	-1.12±0.03
GRB 090529	100	2.625	6.8±1.7	0.06±0.18	1.55±0.5	1.45±0.3	-0.89±0.48	-0.97±0.1	-0.97±0.1

Table 3 continued on next page

Table 3 *(continued)*

GRB Name	T_{90}^{a} (s)	z^{a}	S(15-150 keV)^{a} (10^{-7} erg/cm^2)	α_1^{b}	α_2^{b}	$\log(T_a/10^3)^{b}$ (s)	$\log(L_X/10^{47})^{c}$ (erg/s)	$\log(E'_{\gamma,\rm iso}/10^{53})^{d}$ (erg)	$\log(E_{\gamma,\rm iso}/10^{53})^{e}$ (erg)
GRB 090530	48	1.266	11±1	0.06±0.12	1.08±0.09	0.23±0.2	-0.29±0.26	-1.33±0.04	-1.47±0.04
GRB 090618	113.2	0.54	1050±10	0.48±0.06	1.59±0.06	0.5±0.16	0.2±0.33	-0.1±0	-0.2±0
GRB 090927	2.2	1.37	2±0.3	0±0.19	1.26±0.11	0.6±0.13	-0.49±0.2	-2±0.06	-2.08±0.06
GRB 091018	4.4	0.971	14±1	0.29±0.1	1.27±0.06	-0.53±0.16	0.84±0.2	-1.45±0.03	-1.52±0.03
GRB 091029	39.2	2.752	24±1	0.01±0.09	1.2±0.05	0.38±0.09	0.66±0.18	-0.38±0.02	-0.69±0.02
GRB 091109A	48	3.5	16±2	0.05±0.35	1.04±0.07	-0.76±0.19	1.06±0.21	-0.39±0.05	-0.84±0.05
GRB 091127	7.1	0.49	90±3	0.6±0.19	1.63±0.41	1.03±0.48	-0.22±0.23	-1.25±0.01	-1.24±0.01
GRB 091208B	14.9	1.0633	33±2	0.11±0.14	1.23±0.07	-0.4±0.12	0.58±0.29	-1±0.03	-1.08±0.03
GRB 100219A	18.8	4.7	3.7±0.6	0.21±0.26	4.64±1.44	0.83±0.12	0.28±0.35	-0.83±0.07	-1.33±0.07
GRB 100302A	17.9	4.813	3.1±0.4	0.03±0.15	0.96±0.1	0.22±0.2	0.31±0.25	-0.89±0.05	-1.1±0.05
GRB 100418A	7	0.6235	3.4±0.5	-0.16±0.11	1.43±0.15	1.69±0.12	-1.84±0.11	-2.46±0.06	-2.42±0.06
GRB 100424A	104	2.465	15±1	-0.23±0.25	2.36±0.13	-1.08±0.05	2.51±0.21	-0.67±0.03	-0.76±0.03
GRB 100425A	37	1.755	4.7±0.9	0.22±0.13	1.18±0.16	0.55±0.22	-0.54±0.3	-1.43±0.08	-1.25±0.08
GRB 100513A	84	4.772	14±1	0.24±0.24	1.14±0.2	0.02±0.29	0.77±0.28	-0.24±0.03	-0.53±0.03
GRB 100615A	39	1.398	50±1	0.16±0.07	1.45±0.23	0.86±0.17	0.38±0.22	-0.59±0.01	-0.64±0.01
GRB 100621A	63.6	0.542	210±0	0.47±0.08	1.52±0.11	1.2±0.18	-0.86±0.3	-0.79±0	-0.81±0
GRB 100704A	197.5	3.6	60±2	0.25±0.09	1.41±0.09	0.36±0.14	1.13±0.25	0.2±0.01	0.03±0.01
GRB 100814A	174.5	1.44	90±2	0.37±0.06	2.4±0.27	1.84±0.07	-0.47±0.39	-0.31±0.01	-0.52±0.01
GRB 100901A	439	1.408	21±3	0.01±0.04	1.47±0.04	1.19±0.02	0.1±0.02	-0.96±0.06	-1.14±0.06
GRB 100902A	428.8	4.5	32±2	0.65±0.03	4.69±1.59	2.18±0.07	-0.34±0.16	0.08±0.03	0.07±0.03
GRB 100906A	114.4	1.727	120±0	0.38±0.13	2.5±0.32	0.7±0.15	0.3±0.39	-0.04±0	-0.13±0
GRB 101219B	34	0.5519	21±4	0.11±0.24	0.8±0.11	1.22±0.23	-2.08±0.22	-1.77±0.08	-1.86±0.08
GRB 110213A	48	1.46	59±4	-0.41±0.26	1.95±0.06	0.01±0.08	1.42±0.3	-0.48±0.03	-0.55±0.03
GRB 110715A	13	0.82	118±2	0.35±0.1	0.98±0.01	-0.84±0.09	1.32±0.1	-0.67±0.01	-0.87±0.01
GRB 110808A	48	1.348	3.3±0.8	0.03±0.19	1.18±0.23	1.11±0.27	-1.12±0.3	-1.8±0.09	-1.68±0.09
GRB 111008A	63.46	5	53±3	0.01±0.07	1.39±0.07	-0.06±0.08	1.79±0.19	0.37±0.02	0.26±0.02
GRB 111123A	290	3.1516	73±3	0.24±0.22	1.86±0.3	0.7±0.14	0.51±0.24	0.2±0.02	0±0.02
GRB 111209A	-	0.677	360±10	0.33±0.03	15.11±2.02	1.5±0.06	-1.57±0.48	-0.36±0.01	-0.47±0.01
GRB 111228A	101.2	0.71627	85±2	0.14±0.11	1.32±0.06	0.77±0.09	-0.4±0.16	-0.93±0.01	-0.87±0.01
GRB 111229A	25.4	1.3805	3.4±0.7	-0.14±0.09	3.15±1.13	0.57±0.09	-0.14±0.25	-1.77±0.08	-1.82±0.08
GRB 120118B	23.26	2.943	18±1	-0.17±0.18	1.25±0.22	0.04±0.21	0.79±0.21	-0.46±0.02	-0.41±0.02
GRB 120326A	69.6	1.798	26±3	-0.23±0.13	1.99±0.1	1.26±0.03	0.26±0.05	-0.67±0.05	-0.93±0.05
GRB 120327A	62.9	2.813	36±1	0.08±0.17	1.55±0.12	-0.4±0.12	1.46±0.25	-0.19±0.01	-0.47±0.01
GRB 120404A	38.7	2.876	16±1	0.05±0.17	2.05±0.28	-0.04±0.12	0.91±0.2	-0.53±0.03	-0.62±0.03
GRB 120422A	5.35	0.28	2.3±0.4	0.16±0.12	1.31±0.39	2.07±0.25	-3.46±0.33	-3.35±0.07	-3.44±0.07
GRB 120521C	26.7	6	11±1	0.07±0.19	3.03±1.57	0.51±0.13	0.31±0.27	-0.2±0.04	-0.42±0.04
GRB 120712A	14.7	4.1745	18±1	-0.04±0.41	3.26±1.67	1.65±0.15	-0.55±0.32	-0.22±0.02	-0.67±0.02
GRB 120802A	50	3.796	19±3	0.1±0.11	0.87±0.37	0.18±0.26	0.72±0.27	-0.26±0.06	-0.8±0.06
GRB 120811C	26.8	2.671	30±3	0.3±0.13	1.26±0.17	-0.14±0.17	1.16±0.18	-0.31±0.04	-0.65±0.04

Table 3 continued on next page

Table 3 *(continued)*

GRB Name	T_{90}^{a} (s)	z^{a}	S(15-150 keV)^{a} (10^{-7} erg/cm^2)	α_1^{b}	α_2^{b}	$\log(T_a/10^3)^{b}$ (s)	$\log(L_X/10^{47})^{c}$ (erg/s)	$\log(E'_{\gamma,\rm iso}/10^{53})^{d}$ (erg)	$\log(E_{\gamma,\rm iso}/10^{53})^{e}$ (erg)
GRB 120922A	173	3.1	62±7	0.09±0.24	1.09±0.06	-0.27±0.15	1.3±0.15	0.11±0.05	-0.14±0.05
GRB 121024A	69	2.298	11±1	0.24±0.29	1.52±0.28	0.59±0.18	0.18±0.2	-0.86±0.04	-1.16±0.04
GRB 121128A	23.3	2.2	69±4	0.2±0.19	1.67±0.12	-0.42±0.1	1.58±0.25	-0.09±0.02	-0.43±0.02
GRB 121211A	182	1.023	13±2.67	0.09±0.22	1.32±0.15	0.64±0.16	-0.46±0.22	-1.44±0.08	-1.33±0.08
GRB 130131B	4.3	2.539	3.4±0.4	0.23±0.33	1.47±0.41	-0.56±0.26	1.03±0.3	-1.29±0.05	-1.76±0.05
GRB 130408A	28	3.758	23±4	0.28±0.32	3.79±0.74	0.76±0.07	0.6±0.24	-0.18±0.07	-0.67±0.07
GRB 130420A	123.5	1.297	71±3	0.32±0.13	1.08±0.07	0.2±0.16	0.08±0.22	-0.5±0.02	-0.67±0.02
GRB 130511A	5.43	1.3033	2.2±0.4	0.38±0.13	1.55±0.19	-0.37±0.22	0.08±0.41	-2±0.07	-2.24±0.07
GRB 130514A	204	3.6	91±2	0.01±0.36	1.23±0.07	-0.18±0.2	1.26±0.24	0.39±0.01	0.25±0.01
GRB 130603B	0.18	0.3564	6.3±0.3	0.14±0.11	1.92±0.23	0.37±0.16	-1.06±0.33	-2.69±0.02	-2.85±0.02
GRB 130606A	276.58	5.913	29±2	-0.01±0.19	1.91±0.25	0.14±0.12	1.3±0.23	0.22±0.03	-0.19±0.03
GRB 130612A	4	2.006	2.3±0.5	0.11±0.27	1.44±0.34	0.06±0.24	-0.17±0.26	-1.64±0.09	-2.66±0.09
GRB 131030A	41.1	1.293	290±0	0.54±0.12	1.21±0.03	-0.75±0.09	1.83±0.13	0.11±0	-0.14±0
GRB 131103A	17.3	0.599	8.2±1	0.03±0.19	1.07±0.04	-0.23±0.14	-0.16±0.14	-2.11±0.05	-2.12±0.05
GRB 131105A	112.3	1.686	71±5	0.15±0.13	1.22±0.06	0.23±0.1	0.64±0.1	-0.29±0.03	-0.52±0.03
GRB 140114A	139.7	3	32±1	0.03±0.13	1.48±0.35	0.77±0.18	0.21±0.22	-0.2±0.01	-0.16±0.01
GRB 140206A	93.6	2.73	160±3	0.19±0.08	1.37±0.05	-0.3±0.1	2.06±0.17	0.43±0.01	-0.11±0.01
GRB 140213A	60	1.2076	120±0	0.7±0.08	1.58±0.13	1.28±0.17	-0.18±0.33	-0.33±0	-0.4±0
GRB 140304A	15.6	5.283	12±1	-0.79±0.67	2.38±0.2	-0.99±0.12	2.85±0.38	-0.24±0.03	-0.81±0.03
GRB 140430A	173.6	1.6	11±2	0.03±0.22	1.13±0.25	0.59±0.22	-0.22±0.28	-1.14±0.07	-1.14±0.07
GRB 140512A	154.8	0.725	140±3	0.66±0.04	1.77±0.14	0.99±0.1	-0.12±0.19	-0.71±0.01	-0.84±0.01
GRB 140518A	60.5	4.707	10±1	0.04±0.15	1.7±0.33	-0.31±0.12	1.32±0.24	-0.39±0.04	-1.21±0.04
GRB 140614A	720	4.233	13±4	0.4±0.18	1.64±0.26	0.07±0.21	0.76±0.3	-0.35±0.12	-0.71±0.12
GRB 140629A	42	2.275	24±2	0.37±0.12	1.87±0.17	-0.01±0.21	0.95±0.39	-0.52±0.03	-0.6±0.03
GRB 140703A	67.1	3.14	39±3	0.41±0.14	2.38±0.44	0.53±0.13	1.04±0.36	-0.08±0.03	-0.24±0.03
GRB 140903A	0.3	0.351	1.4±0.1	0.03±0.1	1.56±0.34	0.94±0.19	-1.67±0.21	-3.36±0.03	-3.36±0.03
GRB 141004A	3.92	0.57	6.7±0.3	0.24±0.16	1.87±0.26	0.03±0.17	-0.77±0.3	-2.24±0.02	-2.27±0.02
GRB 141026A	146	3.35	13±1	0.03±0.15	1.65±0.51	1±0.19	0.01±0.24	-0.51±0.03	-0.29±0.03
GRB 141121A	549.9	1.47	53±4	0.06±0.16	2.48±0.5	2.1±0.11	-1.17±0.26	-0.52±0.03	-0.63±0.03
GRB 150323A	149.6	0.593	61±2	0.14±0.17	1.31±0.22	0.84±0.2	-1.45±0.29	-1.25±0.01	-1.28±0.01
GRB 150403A	40.9	2.06	170±3	0.29±0.03	1.44±0.02	-0.31±0.03	2.48±0.09	0.25±0.01	-0.12±0.01
GRB 150423A	0.22	1.394	0.63±0.1	0.08±0.23	1.73±0.75	-0.14±0.49	-0.58±0.51	-2.49±0.06	-2.93±0.06
GRB 150424A	91	3	15±1	0.35±0.09	1.51±0.19	0.91±0.19	-0.03±0.35	-0.53±0.03	-0.99±0.03
GRB 150910A	112.2	1.359	48±4	0.51±0.07	2.47±0.11	0.52±0.04	0.9±0.13	-0.63±0.03	-0.85±0.03
GRB 151027A	129.69	0.81	78±2	0.02±0.05	1.77±0.05	0.37±0.03	0.85±0.08	-0.86±0.01	-0.93±0.01
GRB 151027B	80	4.063	15±3	0.02±0.18	1.33±0.19	0.36±0.21	0.7±0.26	-0.32±0.08	-0.44±0.08
GRB 151112A	19.32	4.1	9.4±1.2	-0.01±0.13	1.67±0.3	0.68±0.21	0.63±0.36	-0.51±0.05	-0.67±0.05
GRB 151215A	17.8	2.59	3.1±0.7	0.21±0.22	1.6±0.67	0.11±0.4	0.32±0.29	-1.32±0.09	-1.32±0.09
GRB 160121A	12	1.96	6.1±0.5	0.02±0.11	1.58±0.61	0.78±0.25	-0.12±0.45	-1.23±0.03	-1.34±0.03

Table 3 continued on next page

Table 3 *(continued)*

GRB Name	T_{90}^{a} (s)	z^{a}	S(15-150 keV)^{a} (10^{-7} erg/cm^2)	α_1^b	α_2^b	$\log(T_a/10^3)^b$ (s)	$\log(L_X/10^{47})^c$ (erg/s)	$\log(E'_{\gamma,\rm iso}/10^{53})^d$ (erg)	$\log(E_{\gamma,\rm iso}/10^{53})^e$ (erg)
GRB 160227A	316.5	2.38	31±2	0.04±0.1	1.43±0.14	0.89±0.14	0.41±0.24	-0.38±0.03	-1.04±0.03
GRB 160303A	5	2.3	1.5±0.3	0±0.21	1.68±0.76	0.65±0.34	-0.78±0.53	-1.72±0.08	-2.23±0.08
GRB 160314A	8.73	0.726	2.8±0.4	0.14±0.28	2.27±1.13	2.09±0.22	-2.56±0.39	-2.4±0.06	-2.52±0.06
GRB 160327A	28	4.99	14±1	-0.22±0.31	1.61±0.15	-0.38±0.13	1.53±0.18	-0.21±0.03	-0.33±0.03
GRB 160804A	144.2	0.736	114±3	0.26±0.17	0.94±0.12	0.78±0.2	-1.07±0.34	-0.78±0.01	-0.93±0.01
GRB 161108A	105.1	1.159	11±1	0.24±0.12	0.95±0.19	1.29±0.21	-1.08±0.39	-1.4±0.04	-1.45±0.04
GRB 161117A	125.7	1.549	200±0	0.1±0.43	1.2±0.06	0.42±0.12	0.44±0.15	0.1±0	-0.23±0
GRB 170113A	20.66	1.968	6.7±0.7	0.08±0.12	1.29±0.06	-0.08±0.1	1.08±0.17	-1.19±0.04	-1.78±0.04
GRB 170202A	46.2	3.65	33±1	-0.42±0.28	1.15±0.05	-0.43±0.1	1.61±0.19	-0.05±0.01	-0.26±0.01
GRB 170519A	216.4	0.818	11±2	0.03±0.17	1.44±0.19	0.47±0.16	-0.32±0.26	-1.7±0.07	-1.72±0.07
GRB 170607A	-	0.557	75±3	0.03±0.1	1.09±0.07	0.89±0.1	-0.8±0.16	-1.21±0.02	-1.29±0.02
GRB 170705A	217.3	2.01	95±3	0.29±0.07	1.29±0.09	0.78±0.12	0.68±0.2	-0.02±0.01	-0.19±0.01
GRB 170714A	-	0.793	28±3	0.54±0.01	4.97±0.16	0.89±0.01	0.97±0.03	-1.33±0.04	-1.39±0.04
GRB 171205A	189.4	0.0368	36±3	-0.05±0.09	1.14±0.15	2.02±0.13	-4.63±0.1	-3.96±0.03	-3.97±0.03
GRB 171222A	174.8	2.409	19±2	0.02±0.13	1.21±0.42	1.47±0.33	-0.72±0.33	-0.58±0.04	-0.55±0.04
GRB 180115A	40.9	2.487	7.6±1.1	0.15±0.14	1.41±0.13	0±0.14	0.68±0.24	-0.96±0.06	-1.14±0.06
GRB 180325A	94.1	2.25	65±2	0.45±0.11	2.38±0.69	0.16±0.27	1.46±0.32	-0.1±0.01	-0.52±0.01
GRB 180329B	210	1.998	33±3	0.03±0.13	1.56±0.16	0.26±0.12	0.42±0.17	-0.49±0.04	-0.98±0.04
GRB 180404A	35.2	1	13±1	0.02±0.13	1.48±0.38	0.89±0.33	-1.09±0.57	-1.46±0.03	-1.47±0.03
GRB 180720B	-	0.654	860±10	0.67±0.09	1.99±0.45	1.33±0.17	0.32±0.49	-0.01±0.01	-0.15±0.01

[a] Taken from the *Swift* GRB Table at https://swift.gsfc.nasa.gov/archive/grb_table.html/.

[b] Fitting results by using Equation (1), carried out through a Markov chain Monte Carlo (MCMC) algorithm

[c] Calculated from Equation (2).

[d] Calculated from Equation (3).

[e] Calculated from Equation (4).

Table 4. The Bromberg criteria test on the "internal plateau" GRBs. Except for two GRBs with T_{90} unavailable (GRBs 111209A and 170714A), all other events are explicitly identified as long GRBs.

GRB name	T_{90}(s)	PL	f_{NC}	Type
GRB 050730	156.5	1.53	0.08 ($< 50\%$)	Long
GRB 060607A	102.2	1.47	0.10 ($< 50\%$)	Long
GRB 070110	88.4	1.58	0.10 ($< 50\%$)	Long
GRB 100219A	18.8	1.34	0.20 ($< 50\%$)	Long
GRB 100902A	428.8	1.98	0.06 ($< 50\%$)	Long
GRB 111209A	–	1.48	–	–
GRB 111229A	25.4	1.85	0.17 ($< 50\%$)	Long
GRB 120521C	26.7	1.73	0.17 ($< 50\%$)	Long
GRB 120712A	14.7	1.36	0.23 ($< 50\%$)	Long
GRB 130408A	28.0	1.28	0.17 ($< 50\%$)	Long
GRB 170714A	–	1.76	–	–

Table 5. Kendall's Tau test for a few pairs of parameters. The coefficients indicate that no significant correlations existed between these parameters.

	τ	p
logT_a - z	-0.24	2.55e-6
log$E_{\gamma,\rm iso}$ - logT_a	-0.11	0.038
α_1 - α_2	0.03	0.57
logL_X - α_1	0.11	0.024
logT_a - α_1	-0.11	0.028
log$E_{\gamma,\rm iso}$ - α_1	0.12	0.019
logL_X - α_2	0.04	0.41
logT_a - α_2	0.16	0.002
log$E_{\gamma,\rm iso}$ - α_2	0.13	0.014
logL_X - logT_{90}	0.06	0.22
logT_a - logT_{90}	0.17	0.0008